01 Jan 2020

Microwave Camera for Concrete Delamination and Steel Corrosion Detection -- Final Project Report

Chao Liu

Mohammad T. Al Qaseer

Reza Zoughi

FINAL REPORT #_____

GRANT NO: 69A3551747126
GRANT PERIOD: 11/30/16 – 06/30/22
PROJECT PERIOD: _

Inspecting and Preserving Infrastructure through Robotic Exploration (INSPIRE)

Tier 1 University Transportation Center Sponsored by the Office of the Assistant Secretary for Research and Technology (OST-R)

Project/Report Title:	Microwave Camera for Concrete Delamination and Steel Corrosion Detection
Consortium Member:	Iowa State University
Principal Investigator:	Dr. Reza Zoughi
Co-Principal Investigator(s):	
Report Authors:	C. Liu, M.T. Al Qaseer and R. Zoughi

Missouri S&T · The City College of New York · Georgia Tech · UNLV · East Central College · Lincoln · Ozarks Technical Community College · St. Louis Community College

DISCLAIMER

The contents of this report reflect the views of the authors, who are responsible for the facts and the accuracy of the information presented herein. This document is disseminated in the interest of information exchange. The report is funded, partially or entirely, by a grant from the U.S. Department of Transportation's University Transportation Centers Program. However, the U.S. Government assumes no liability for the contents or use thereof.

TECHNICAL REPORT DOCUMENTATION PAGE

1. Report No. INSPIRE UTC #	**2. Government Accession No.** (blank)	**3. Recipient's Catalog No.** (blank)
4. Title and Subtitle Microwave Camera for Concrete Delamination and Steel Corrosion Detection		**5. Report Date** June 30, 2020 **6. Performing Organization Code**
7. Author(s) C. Liu, M.T. Al Qaseer and R. Zoughi		**8. Performing Organization Report No.** Project #_____
9. Performing Organization Name and Address RE-CAST – Missouri S&T 500 West 16th Street Rolla, MO 65409-0710		**10. Work Unit No.** (blank) **11. Contract or Grant No.** USDOT:
12. Sponsoring Agency Name and Address Office of the Assistant Secretary for Research and Technology U.S. Department of Transportation 1200 New Jersey Avenue, SE Washington, DC 20590		**13. Type of Report and Period Covered** Final Report Period: 9/1/2019-6/30/2020 **14. Sponsoring Agency Code**
15. Supplementary Notes The investigation was conducted in cooperation with the U. S. Department of Transportation.		

16. Abstract

This project studied the capability of microwave methods to detect thickness of induced corrosion byproduct on rebars embedded into concrete, and also similarly embedded delamination. Three microwave methods used or investigated included microwave synthetic aperture radar (SAR) imaging method, microwave resonance method, and microwave nonlinear measurement. Wideband, low-frequency antennas including a double-ridged horn and a Vivaldi antenna were designed for achieving reasonable spatial resolution while being able to penetrate lossy concrete. Simulations and experiments were conducted for all of these investigations. For the rebar samples use, the results showed that the corrosion thickness was very small (~50 μm) which seemed to be out of the resolution capabilities of the microwave imaging method. Microwave resonance method initially showed good indications based on the relationship between the resonant frequency and the corrosion thickness by simulation results, but it does not work when the corrosion thickness is below 1% for a rebar with a radius of 7.9 mm. Microwave nonlinear measurement method brings positive indications based on the results from the initial experiments, which showed that the metal-insulation-metal junction can produce relatively measurable harmonic power and the value of it is proportional to the insulation thickness. Microwave imaging method for concrete delamination detection were also examined by measurements. It was found that the antenna beam has significant effect on cross-range and range resolutions. This had not been previously investigated and was hence studied comprehensively with a significant journal paper (recently) submitted for possible publication

17. Key Words Microwave NDE, SAR Imaging, Resolution	**18. Distribution Statement** No restrictions. This document is available to the public.	
19. Security Classification (of this report) Unclassified	**20. Security Classification (of this page)** Unclassified	**21. No of Pages**

Form DOT F 1700.7 (8-72) Reproduction of form and completed page is authorized.

EXECUTIVE SUMMARY

In this project, measurement techniques including microwave imaging method, microwave resonance method, and microwave nonlinear measurement method, for estimating the thickness of the induced corrosion byproduct of rebar embedded into concrete were studied, proposed, and verified by simulations and measurements. And the capability of microwave imaging system to detect delamination with different scattering properties was investigated.

In order to provide enough penetration depth and higher resolution, a wideband and low-frequency double-ridged horn and a Vivladi antenna were designed and fabricated and used in synthetic aperture radar (SAR) imaging measurements. The sensitivity of different methods to the corrosion thickness was analyzed and results show that microwave imaging method and microwave resonance method may not have enough resolution, while microwave nonlinear measurement may be a good candidate based on the initial measurement results. Point target simulations were conducted to study the antenna pattern effect on cross-range and range resolutions as well (not been studied before), which showed that this pattern effect is responsible for tuning the sensitivity of SAR system to the scattering properties of the delamination and other targets.

ACKNOWLEDGMENT

Financial support for this INSPIRE UTC project was provided by the U.S. Department of Transportation, Office of the Assistant Secretary for Research and Technology (USDOT/OST-R) under Grant No. 69A3551747126 through INSPIRE University Transportation Center (http://inspire-utc.mst.edu) at Missouri University of Science and Technology. The views, opinions, findings and conclusions reflected in this publication are solely those of the authors and do not represent the official policy or position of the USDOT/OST-R, or any State or other entity.

Table of Contents

Chapter 1 DESCRIPTION OF THE PROBLEM 8
Chapter 2 2. APPROACH 9
2.1 Microwave SAR imaging 10
2.1.1 Basic principle 10
2.2.2 Multi-layer SAR algorithm 11
2.2.3 SAR performance considerations for corrosion detection 12
2.2.4 SAR performance considerations for concrete delamination detection 14
2.2 Microwave resonance of periodic structure 14
2.3 Microwave nonlinear harmonics 15
Chapter 3 3. METHODOLOGY 16
3.1 Fabrication of concrete samples 16
3.2 Cyclical corrosion procedure 19
3.3 Antennas for scanning 21
3.4 Microwave imaging in cyclical corrosion 21
3.4.1 Sample group 1 21
3.4.2 Sample group 2 24
3.4.3 Sample group 3 27
3.4.4 Rebar in air 30
3.5 Rebar corrosion simulation for microwave imaging 31
3.5.1 Sensitivity to corrosion thickness 31
3.6 Resonance simulation for periodically distributed rebars 35
3.6.1 Rebar in air 35
3.6.2 Rebar embedded in concrete 36
3.7 Harmonic measurement on cyclically corroded rebar 38
3.8 Bridge delamination detection 41
3.9 Simulated delamination detection 45
3.9.1 Concrete casting with delamination 45
3.9.2 Antennas for scanning 46
3.9.3 Imaging results and analysis 55
3.9.4 Antenna pattern effect on SAR sensitivity to delamination 61
Chapter 4 FINDINGS 72

4.1 Sensitivity of microwave SAR imaging technique to corrosion thickness 72
4.2 Sensitivity of microwave SAR imaging technique to concrete delamination 73
4.3 Sensitivity of microwave harmonic measurement to corrosion detection 73
Chapter 5 5. CONCLUSIONS 74
Chapter 6 6. RECOMMENDATIONS DEVELOPED AS A RESULT OF THE PROJECT 74
Chapter 7 References 74

[INSTRUCTIONS: Final research reports must give a complete description of the problem, approach, methodology, findings, conclusions, and recommendations developed as a result of the project and must completely document all data gathered, analyses performed, and results achieved. *Please remove the instructions after completing the report.*]

Chapter 1 **DESCRIPTION OF THE PROBLEM**

It is known that corrosion of reinforcing steel bars (rebars) embedded in concrete is a significant maintenance, rehabilitation and safety issue as it relates to the overall health of concrete structures, particularly those subjected to cyclical chloride attack, including roadways, bridges and dams [1]. And corrosion byproducts (i.e., rust) occupy a larger volume than the materials that produced it, leading to stresses that can cause cracking and spalling, and delamination in these structures, followed by increased salt and moisture permeation and further damage. Invisibility of the embedded rebar in combination with physical inaccessibility in elevated bridges presents a challenge in the assessment of RC bridge elements.

Consequently, it is critical to devise a robust detection and evaluation techniques to monitor degradation of these structures, such as concrete delamination, and defects due to rebar corrosion. Theoretical modeling results predicting corrosion rates are not always corroborated by experimental verifications as pointed out by [2] and [3], and there exist significant discrepancies in accuracy associated with different testing methods [4]. For studying the effect of corrosion, electrochemical testing technique is a method of inducing corrosion on an embedded rebar with reasonable control of the corrosion growing process [5] [6]. This process can then be combined with different testing techniques to evaluate their efficacy for detecting and assessment of corrosion level. Meanwhile, concrete delamination, another major concern in building health inspection, has not been well-solved as well. Current techniques, such as acoustic and Infrared thermography, are either requiring the contact between the sensor and the concrete surface or cannot penetrate a lot.

Wideband microwave imaging, using synthetic aperture radar (SAR) techniques, has shown great potential for producing 3D images of structures containing rebars or different kinds of delamination or voids. The principle is that microwave signals can propagate through concrete and be differently reflected by steel reinforcing bars, delamination and voids based on their reflectivity. Such reflectivity is then used to identify the properties of these infects. More specifically, for corrosion detection, steel corrosion byproduct (i.e., rust) is with a relatively high permittivity and high loss dielectric material, which results in the absorption of the irradiating microwave energy, leading to rebar image becoming less prominent. Reversely, for concrete delamination detection, the permittivity is usually smaller than that of concrete, leading to a highlighted indication in the final image. Hence, high-resolution images of concrete samples subjected to accelerated corrosion or the existence of different kinds of delamination are expected to result in a better understanding and limitations of this imaging approach.

Although the principle of microwave SAR imaging in NDE applications has been well-documented and a great promise has been shown, a methodical approach to investigate the overall efficacy of this imaging technique has not yet taken place. In order to accomplish this aim, a SAR imaging system with high performance, such as good resolution and large signal-to-noise ratio, is studied, designed and fabricated by this project.

Chapter 2 **2. APPROACH**

The operation principles of the approaches used in corrosion and delamination detection are described in this section. Specifically, for corrosion detection, approaches include: microwave synthetic aperture radar (SAR) imaging, microwave resonance of periodic structures, and microwave non-linear measurement. For delamination detection, the above microwave SAR imaging is utilized. Details for these methods are given below.

2.1 Microwave SAR imaging

The concept of synthetic aperture has been widely used in many areas and applications due to its various inherent benefits including generation of high-resolution images. The techniques is also non-contact and the results may be combined with other NDE data for enhanced detection and evaluation.

2.1.1 Basic principle

The principle schematic of SAR imaging process is given in Figure 2-1. This imaging techniques benefits from advances made in synthetic aperture radar (SAR) imaging developments over the past several decades. The approach involves scanning a small antenna over a structure under inspection. During the scan, the distance from the antenna to the anomaly (rebar) changes, and correspondingly the phase of the detected reflected signal. Subsequently, this phase is recorded for all antenna locations that illuminate the anomaly. By mathematically compensating for the phase differences among the recorded signals (i.e., back-propagation, Omg-k algorithm), effectively a larger antenna (i.e. with finer resolution) is *synthetically produced*, or that all of the recorded signals are coherently added and are focused on the anomaly, as shown in Figure 2-1 [7]. A 2D scan of the structure or using a 2D array of antennas (in lieu of mechanical scanning), produces a high-resolution 2D image, while sweeping over a large transmitted signal bandwidth provides for high-resolution depth information, leading to a 3D image of the structure. The attainable spatial resolution is a function of the scan dimensions, and the target height (all relative to wavelength), while the depth resolution is inversely related to the operating signal bandwidth. Given the fact that image data is coherently averaged over a wideband of frequencies, the signal-to-noise ratio (S/N) associated with such images is relatively high, translating to a relatively high image fidelity.

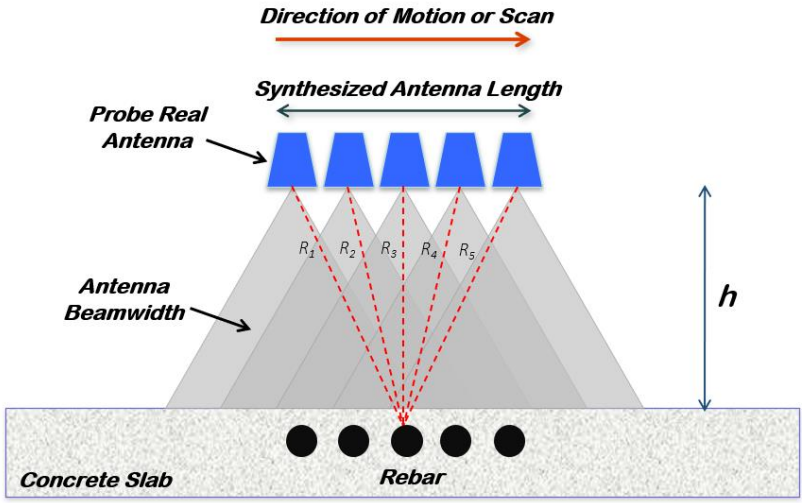

Figure 2-1: Working principle of microwave SAR imaging for rebar corrosion detection.

Finally, the reflectivity ($\Gamma(x, y, z)$) of the entire concrete section can be reconstructed by the following equation:

$$\Gamma(x', y', z'-z) = FT_{xyz}^{-1}\left[\bar{S}(K_x, K_y, K_z, z)\cdot \exp(jK_z z)\right] \quad (1)$$

in which K_x, K_y and K_z are the wavenumbers in each coordinate direction, and z is the depth location of the slice within the reconstructed 3D image [7].

2.2.2 Multi-layer SAR algorithm

In the case of a layered structure a more complex formation will be needed to produce proper SAR images. The Green's function-based SAR has been developed for such cases [7]. Therefore, for the concrete model, since the antenna used for scanning is always placed within air and the rebars are embedded into concrete, it is always necessary to use this multilayer SAR algorithm. The details of this algorithm can be found in [7] and will not be repeated here.

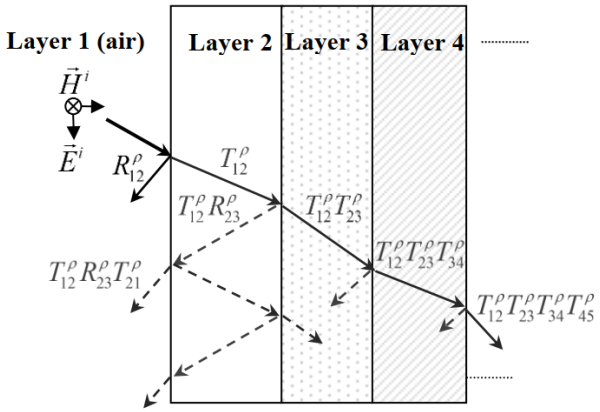

Figure 2-2: Multilayer interactions of electromagnetic waves.

Finally, the reflectivity (Γ) of the concrete to be reconstructed and the measured reflection coefficients ($\bar{S}$) have the following relationship based on the wiener filter used:

$$\Gamma(x', y', z', f) = FT_{xy}^{-1}\left\{\frac{\bar{S}\cdot(\bar{G}^P)^H}{\bar{G}^P\cdot(\bar{G}^P)^H + \delta^2}\right\} \quad (2)$$

in which $\bar{G}^P$ is the Green's function in frequency domain, δ is the power density of the noise in the measurement system and FT_{xy}^{-1} means the two-dimensional inverse Fourier transform along xy plane, which is the plane of the synthetic aperture [7].

2.2.3 SAR performance considerations for corrosion detection

The performance of a SAR system can be mainly characterized by the cross-range resolution and the range resolution, which set the limit in corrosion byproduct thickness detection. And it has been known that the cross-range (noted as δ_x) and range resolution (noted as δ_z) can be approximated by [8]:

$$\delta_x = \frac{\lambda_c}{4\sin(\theta)},\ \delta_z = \frac{c}{2B} \quad (3)$$

in which λ_c is the wavelength in terms of the center frequency and B is the bandwidth, c is the speed of light, and θ is the effective integration angle which is the smaller one between the antenna beamwidth

and the aperture angle [9]. In this case, the parameters that are responsible for resolution control can be mainly classified into two categories: antenna-related and aperture-related.

(a) Antenna

This includes the frequency bandwidth and frequency sampling density, the gain pattern and its half power beamwidth (HPBW). For the frequency related effect, its sampling step is always required to be as small as possible for high resolution. And the frequency used should be as high as possible for better cross-range resolution according to equation (3). But lower frequencies provide larger penetration depth which is also required for corrosion detection since the rebar is embedded into (lossy) concrete with about 60 mm distance to the concrete surface. Consequently, the frequency selected should be a compromise between resolution and depth of penetration, which was studied by using antennas operating in different frequency bands. Meanwhile, the signal bandwidth is also important for range resolution as given in equation (3), but as just mentioned, high frequencies do not propagate deep into the concrete. For antenna pattern related effects, it is also confirmed that antennas with wide beams can produce higher cross-range and range resolution while larger gain can increase the signal-to-noise ratio. But this two cannot be maximized as the same time and is hence also a compromise.

(b) Synthetic aperture

Apart from the antenna used, the synthetic aperture is another key factor that influences the performance of a SAR system in corrosion detection. Generally, there are two related parameters: the total length of the synthetic aperture and its sampling step. Length of the synthetic aperture, for a given standoff distance, *h*, affects the cross-range resolution and this issue has been well studied previously [9]. However, the influence of the antenna gain pattern on cross-range and range resolutions of SAR images, specifically for NDE applications, has not been investigated. These two issues are also studied in

this project. The frequency sampling is important from the perspective of properly reconstructing the image and also it sets the largest distance away from the synthetic aperture that data can be collected.

Consequently, to detect the corrosion byproduct on the surface of the embedded rebars, the requirements on the antenna used include wideband for high resolution, lower starting frequency for larger penetration depth, and sufficient frequency sampling. For the synthetic aperture, both relatively longer synthetic aperture in terms of the depth distance where the rebar is located, and sufficient frequency sampling need to be used.

Moreover, since SAR imaging is a phase-based reconstruction algorithm, the calibration of phase is also very important. Open-ended waveguide radiators (probes) can be easily calibrated (referenced to their apertures) using standard loads and techniques, unlike a horn antenna. Therefore, waveguides in X-band (8.2-12.4 GHz) and G-band (3.95-5.85 GHz) were primarily used in this investigation as the scanning antenna.

2.2.4 SAR performance considerations for concrete delamination detection

Apart from the advantages mentioned in section 2.2.3, the difference between corrosion detection and delamination detection is that the former is more of a localized (point) target and the latter is a planar target. Small voids do not reflect a strong signal and are more difficult to detect. In this case, the sensitivity of a SAR system to weak-scattering objects nearby a strong scattering target was also studied in this project.

2.2 Microwave resonance of periodic structure

Another method that has potential to detect corrosion was also briefly investigated, which is based on the concept of frequency selective surfaces (FSS). Figure 2-3 shows that an element structure is periodically copied and distributed with same distance in each direction [10].

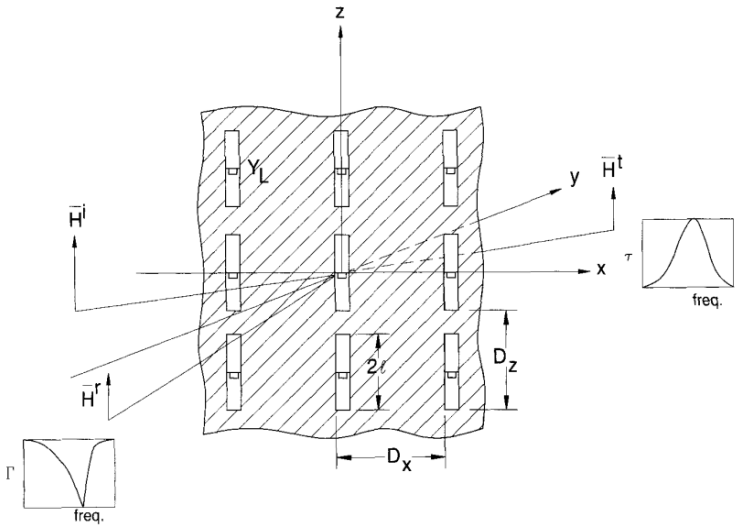

Figure 2-3: Microwave resonance of a periodic structure.

Specifically, when an electromagnetic wave illuminates the structure, the energy at the resonant frequency is totally transmitted while for waves with frequencies far away from the resonant frequency, they are totally reflected. In this case, the resonant frequency is the key point for corrosion detection since it is highly dependent on the geometry of the structure and the distribution of the embedded rebars is usually periodic. Hence, when the rebar is gradually corroded, its radius is gradually reduced and the corrosion thickness increases, which may lead to the shift in the resonant frequency of the entire structure. Therefore, the sensitivity of such a technique to corrosion thickness was also examined in this project.

2.3 Microwave nonlinear harmonics

The third method that was investigated for corrosion detection is based on nonlinear measurements. It is based on the concept that the metal-to-metal junctions can be considered a “nonlinear” junction. That means, similar to other nonlinear electronic devices (i.e., a diode), when the junction is illuminated with a high frequency signal, the reflected signal includes harmonic frequency components [11]. The presence of a corrosion layer between two rebars (at their crossing junction) reduces this nonlinear

effect and could be a potential technique for detecting the corrosion. This principle can be explained as follows. As can be seen from Figure 2-4, the left figure shows the physical model of the metal-insulation-metal junction which is exactly the same phenomenon in rebar corrosion. The right figure is the diode tunneling effect explanation, which illustrates that if the thickness of the insulation is very small satisfying the electron tunneling criterion, then this junction can be seen as a diode that has a nonlinear I-V curve with small-signal input.

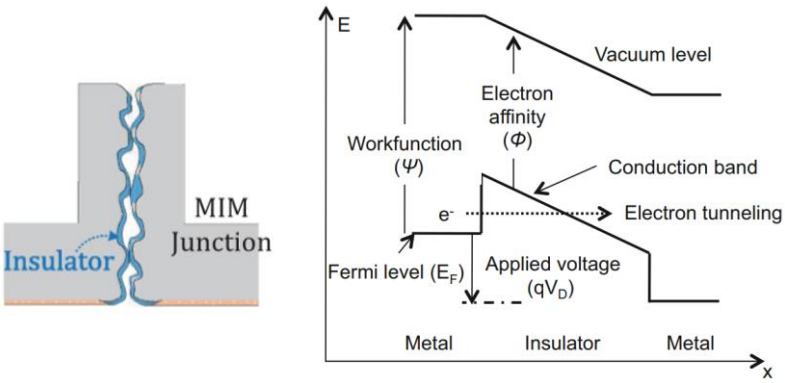

Figure 2-4: Metal-insulation-metal (MIM) physical model (left) [12] and the corresponding electron tunneling effect model for MIM structure (right) [13].

Therefore, some preliminary measurements were also conducted in this project using this technique.

Chapter 3 **3. METHODOLOGY**

3.1 Fabrication of concrete samples

To study the corrosion detection performance of a SAR system, many parameters should be considered, such as the frequency band selected, the corrosion process, the cover thickness of the concrete (the depth distance of the embedded rebar with respect to the concrete upper surface), the dielectric constant of the concrete, which is related to the water-to-cement (w/c) ratio of the concrete. To this end, several groups of concrete samples were cast. The first group is shown in Figure 3-1. The concrete with two embedded rebars was made of cement, sand, and water, with a water-to-cement

ratio of 0.55 and a sand-to-cement ratio of 2.81. The sample was scanned at different frequency bands to make an initial determination of a proper frequency band to be used.

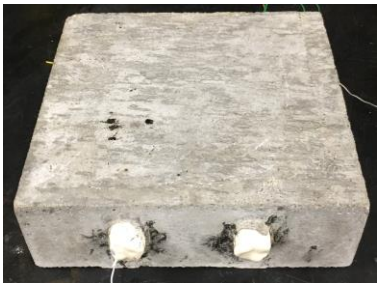

Figure 3-1: Original concrete block with embedded rebars.

Then, another set of six concrete samples were cast. These samples are classified with three cover thicknesses (1", 1.5", and 2") and two water-to-cement (w/c) ratios (0.55 and 0.40) to test the influence of these two parameters to the produced SAR images. One of the fabricated samples is shown in Figure 3-2.

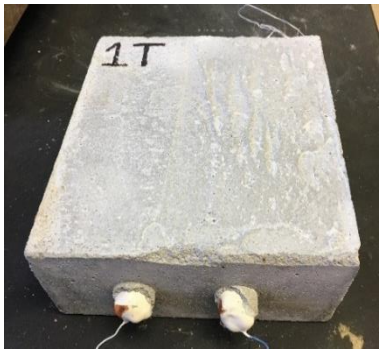

Figure 3-2: Sample with 1" cover, 55% W/C.

Next, since the corrosion process (introduced later) applied to the above samples cannot bring a uniform level of corrosion for the whole rebar, a new corrosion process was devised and implemented, and subsequently another four concrete samples were cast. There are two sets of mortar samples, M1 and M2, with water-to-cement ratios (w/c) of 0.55 and 0.40 and three reinforcing steel bars embedded in each. The mix proportions of the mortars are shown in Table 3-1. After casting, the specimens were

covered with wet burlap and plastic sheet to prevent surface cracking due to drying shrinkage. The specimens were demolded after 24 hours, and then cured in an environmental chamber for 28 days. Subsequently, they were placed in a temperature-controlled room, at 70°C and for approximately 20 days, to remove any excess moisture. Figure 3-3 shows pictures of the form with three rebars and the cast sample, respectively. Dimensions of the final mortar are 42.5 cm (L), 26.5 cm (W) and 12 cm (H). The mortar cover thickness is 5 cm and the rebars are one-foot long with a dimeter of 1.91 cm.

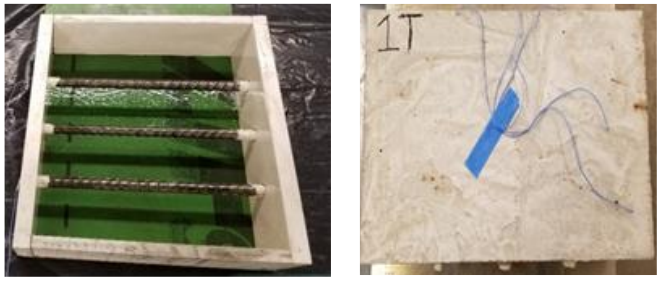

Figure 3-3: Pictures of casting frame (top left), one of the samples (top right) [14].

Table 3-1: Mix proportions of the two mortar mixtures.

Types of mortar	M1	M2
Water	0.55	0.4
Ordinary Portland cement	1.0	1.0
Missouri river sand	2.81	1.83

In addition to these four concrete blocks, eight small samples were also prepared for measuring their dielectric properties, using a completely-filled waveguide approach [15]. This information is important when processing the image data to produce images of the interior of these blocks. These small concrete samples have been cast, cured, and dried. Figure 3-4 shows the samples cast for this purpose.

Miniature Casting Frames

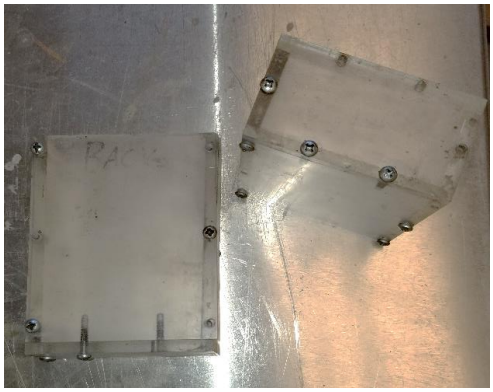

Four Miniature Samples

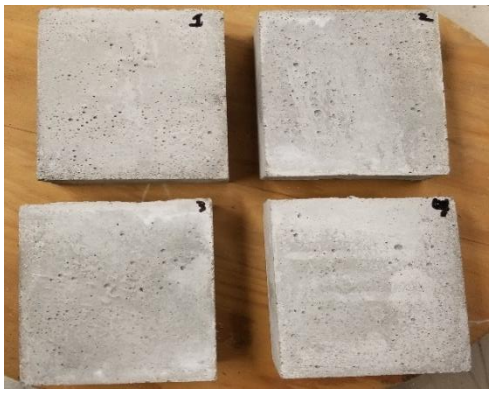

Figure 3-4: Casting frames (left) and four of the eight samples (right).

3.2 Cyclical corrosion procedure

The corrosion procedure for these samples are similar. For the first two sets of samples with two embedded rebars, each sample was placed in a saltwater (NaCl solution) bath with a salinity of 3.5% (by wt.). The saltwater level was kept 0.5 cm lower than the lower edge of steel bars in order to avoid electrical short-circuit between the extruded steel rod and the saltwater solution. However, when a current was sent through these rebars for corrosion, the resulting corrosion was not uniform. To correct this, a new procedure and device was developed and implemented in which a constant current of 500 $\mu A/cm^2$ was impressed through the rebars on both sides to accelerate corrosion until the mass loss of the steel bar reached 0.1%. No current was passed through the middle rebar for the final cast four concrete samples with three rebars embedded. In this way, the middle rebar image could be used as a reference with which to compare the other two rebar images. Subsequent to each soaking cycle, the sample was removed and placed in the temperature-controlled room to remove the excess water. Each day the mass of the sample was measured until such time there was no appreciable change in the mass.

Figure 3-5: Corrosion salt bath setup with corrosion box centered on top.

The flow-chart of the entire experimental process is illustrated in Figure 3-6, which shows that starting from the top block, the procedure was: scan sample @ X-band (8.2-12.4 GHz) & J-band (5.85-8.2 GHz); perform the electrochemical process to produce corrosion; retrieve corroded sample from salt water; send corroded sample to the furnace; take sample out of furnace once the daily sample mass measurements have leveled off.

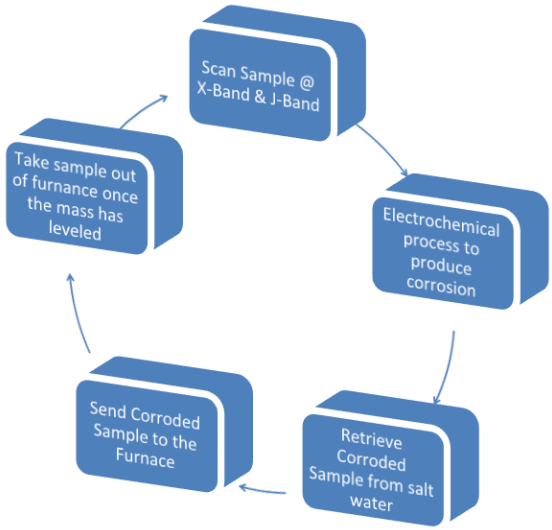

Figure 3-6: Flow-chart of the cyclical electrochemical corrosion and scanning procedure.

3.3 Antennas for scanning

As mentioned in section 2.2.3, for the selection of bandwidth, the low frequency can bring larger penetration depth but also bad cross-range resolution, while wider bandwidth can bring better range resolution, but the high frequency part may not have enough penetration depth. In this case, the open-ended rectangular waveguides, operating in J-band (5.85-8.2 GHz), X-band (8.2-12.4 GHz), Ku-band (12.4-18 GHz) and Ka band (26.5-40 GHz), are taken as the sensors. The geometry of the waveguide is given in Figure 3-7.

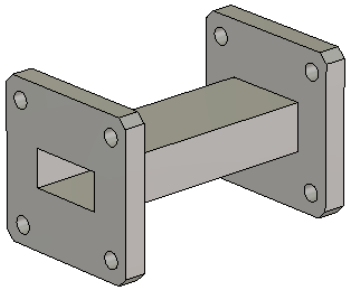

Figure 3-7: The general geometry of the waveguides used in scanning.

3.4 Microwave imaging in cyclical corrosion

In this case, based on the above analysis, the parameters influencing the sensitivity to detect corrosion thickness are evaluated by using different groups of concrete samples. Hence, sample group 1 was imaged to compare the effect of different frequency. Sample group 2 was imaged to study the influence of cover thickness and water-to-cement (w/c) ratio. And sample group 3 was finally cast to study the detection ability under cyclical corrosion procedure.

3.4.1 Sample group 1

To show the effect of different frequency bands used, both (electromagnetic) simulations and measurements were performed. First, for simulations using CST Microwave Studio^{R}, both X-band (8.2-12.4 GHz) and Ku-band (12.4-18 GHz) are used. Ka-band (26.5-40 GHz) was not used since the simulation time is excessively long. The electromagnetic properties of the corrosion (ε_r = 12.5 – j2.3) used in the

simulation were found from previous published measurements made [7], [16], and the depth of the rebar in the concrete was 1 inch. The concrete block was simulated with two embedded rebars and various thicknesses of corrosion. The corrosion was only applied to the rebar on the right side of the block so that a comparison between the corroded and uncorroded rebar could be made, two different corrosion thicknesses of 1.3 mm and 2.6 mm were simulated to study its effect on the images. Produced images are shown in Figure 3-8 and Figure 3-9. As can be seen in Figure 3-8 with 1.3 mm corrosion thickness, the corroded and uncorroded rebar indications look very similar to each other in both images, with the corroded rebar indication slightly faded only in the Ku-band (12.4-18 GHz) image. Then, in Figure 3-9, the indication for corroded rebar becomes clearer for both X-band (8.2-12.4 GHz) and Ku-band (12.4-18 GHz). These results are expected, since corrosion is a lossy dielectric. A thicker layers of corrosion causes more of the signal that would otherwise be reflected back by the rebar to be absorbed.

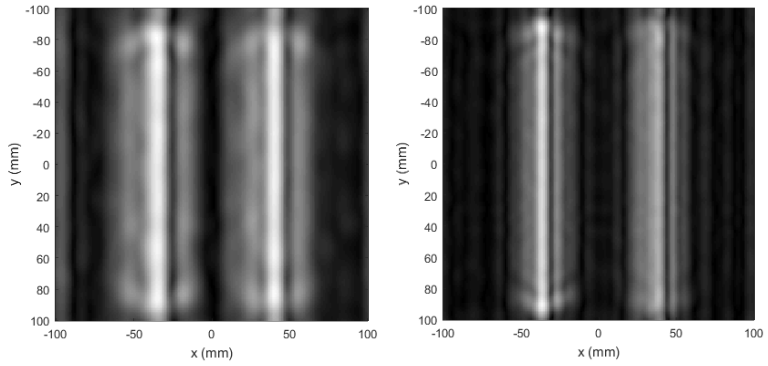

Figure 3-8: Simulated images with 1.3 mm corrosion thickness at X-band (8.2-12.4 GHz) (left) and Ku-band (12-18 GHz) (right). In both images, the left rebar has no corrosion for comparison.

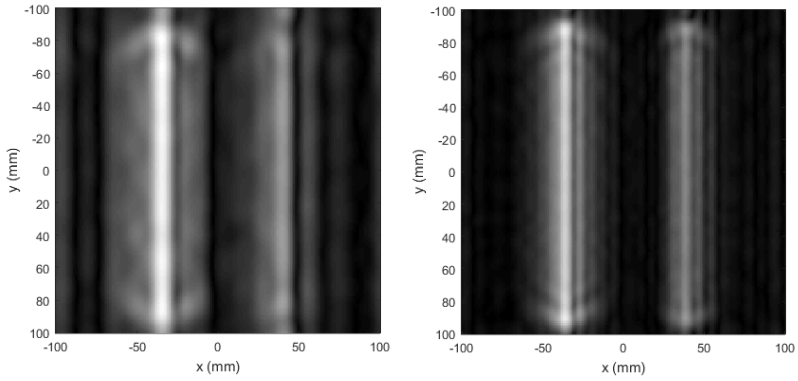

Figure 3-9: Simulated images with 2.6 mm corrosion thickness at X- band (8.2-12.4 GHz) (left) and Ku-band (12-18 GHz) (right). In both images, the left rebar has no corrosion for comparison.

Then, to confirm the simulation results, measurements were conducted on the samples in group 1. These samples were scanned and imaged after each episode of corroding. Results are shown below in Figure 3-10. First, for the original samples with no corrosion, as can be seen from Figure 3-10, X-band, Ku-band and Ka-band waveguides were used to do raster scanning and SAR images were produced. It can be seen that the image produced at X-band (8.2-12.4 GHz) shows clearest indications of the rebar while in the images from Ku-band (12.4-18 GHz) and Ka-band (26.5-40 GHz), rebars are not clearly indicated. Reason for this is that higher frequency cannot provide enough penetration depth due to the fact that concrete is lossy material. And this is different from the above simulations which show that even in Ku-band (12.4-18 GHz), the rebars can be fairly easily detected in the produced images. Reason for this may be that the dielectric constant used in the simulations is not exactly same as in the concrete samples used in scanning at Ku-band (12.4-18 GHz), which is influenced by several parameters such as drying time (in microwave oven), etc. Moreover, the real concrete samples are actually not homogenous as used in simulations. Hence, noise level is larger in measurement. Nevertheless, it can still be found that X-band (8.2-12.4 GHz) is robust for these measurements.

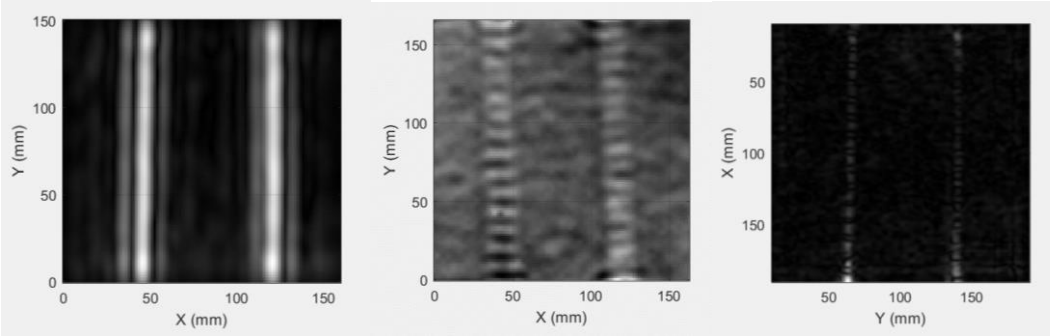

Figure 3-10: Images of the original concrete block (prior to soaking) at X-band (8.2-12.4 GHz) (left), Ku-band (12-18 GHz) raw data (middle), and Ka-band (26.5-40 GHz) (right).

Therefore, the cyclically-corroded rebars in these samples were scanned using the X-band (8.2-12.4 GHz) waveguide and the produced images are shown in Figure 3-11. Again, the left rebar is left uncorroded as reference and the right rebar was gradually corroded. As can be seen from Figure 3-11, from the left figure to the middle and the right figure, the degradation induced by corrosion can be clearly detected.

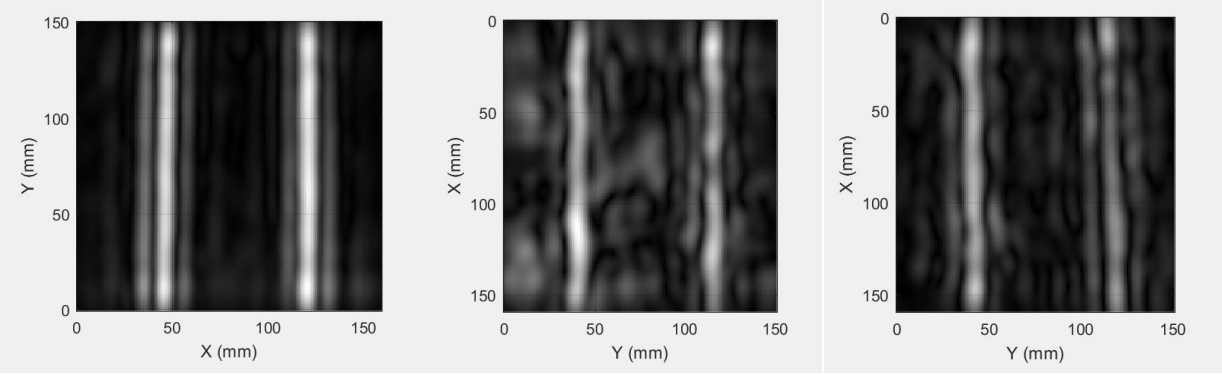

Figure 3-11: X-Band (8.2 – 12.4 GHz) images of the block before soaking (left), after a single soaking cycle (middle), and after two soaking cycles (right).

3.4.2 Sample group 2

Then, to study the influence of cover thickness and water-to-cement (w/c) ratio of concrete, six new concrete blocks, with embedded rebars, were cast with three cover thicknesses of 1”, 1.5”, and 2” and with two water-to-cement (W/C) ratios of 0.55 and 0.40. Subsequently, microwave imaging experiments were performed on each block. Imaging was performed at X-band (8.2-12.4 GHz) and J-

band (5.85 – 8.2 GHz), as the former band was previously determined to be suitable for these experiments and the latter band was also used to study its potential performance for corrosion detection purposes.

To this end, one of the cast concrete samples with 1" cover thickness and 0.55 w/c is displayed in the left figure while the produced images from measurements at J-band (middle) and X-band (right) to this sample are also given, all in Figure 3-12. As can be seen, the two rebars are clearly indicated in each image. The indications at the J-band image appear to be wider than in the X-band image. This is expected, as the image cross-range resolution increases at higher frequencies (X-band).

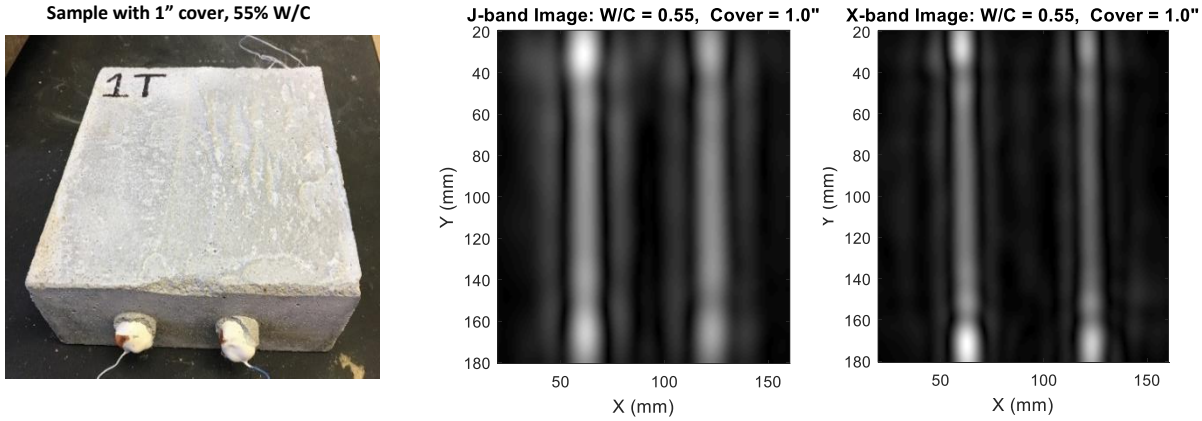

Figure 3-12: The first of six blocks (left), image at J-band (5.85-8.2 GHz) (middle) and X-band (8.2-12.4 GHz) (right).

The effect of each parameter (w/c and cover thickness) on the images was investigated. For X-band (8.2-12.4 GHz) images, increasing the cover thickness of concrete (above the rebar) tends to make the rebar indications less visible. This is expected since concrete is lossy and attenuates the signal. Figure 3-13 shows this effect, where the thicker cover causes the rebar indications to be less distinguishable from the background, as can be seen in the right-most image.

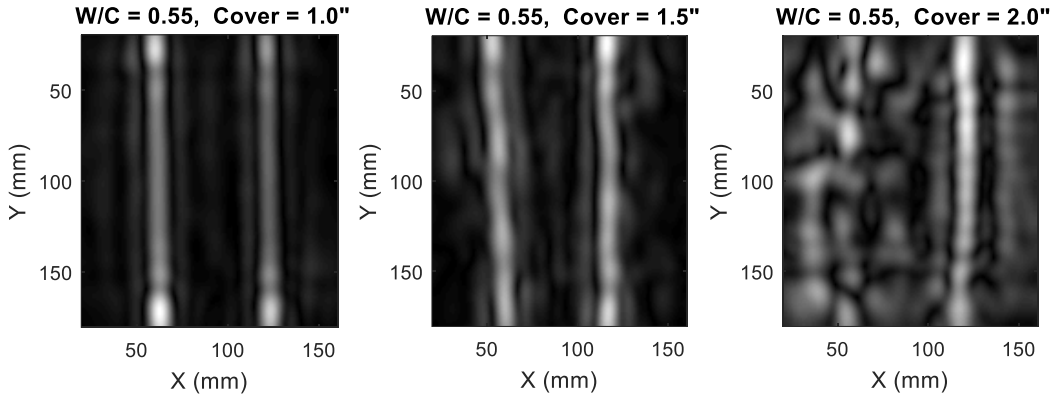

Figure 3-13: X-Band (8.2-12.4 GHz) Images of the blocks with varying cover thickness.

The effect of the cover thickness can be reduced by imaging the block at a lower frequency range, due to signal attenuation at lower frequencies. Figure 3-14 shows the corresponding J-band (5.85-12.4 GHz) images, and the rebar indications can still be clearly seen even with the maximum cover thickness.

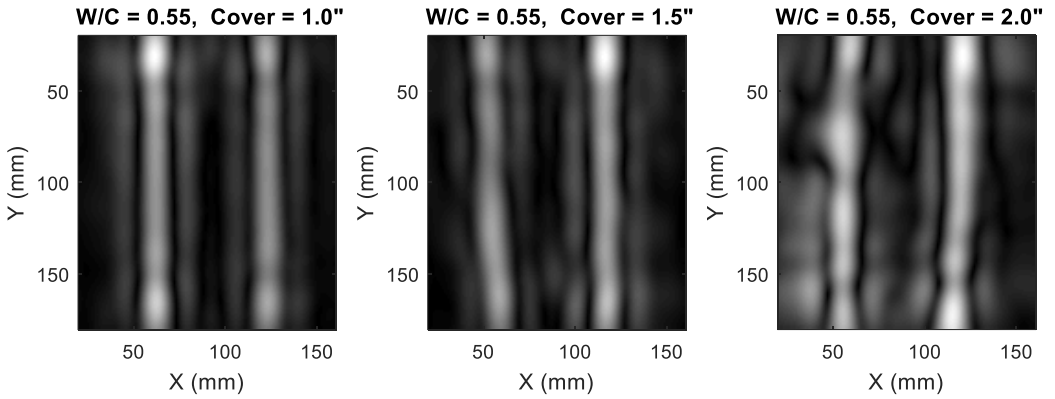

Figure 3-14: J-Band (5.85-8.2 GHz) Images of the blocks with varying cover thicknesses.

Water-to-cement (w/c) ratio also has an effect on rebar indication visibility, due to the fact that samples at lower (w/c) have higher dielectric constant and loss factor. The microwave imaging experiments were performed for two different (w/c) of 0.55 and 0.40. The X-band (8.2-12.4 GHz0 images, shown in Figure 3-15, indicate a noticeable reduction in rebar visibility for the lower w/c. This result is expected as explained in [1], since the higher (w/c) results in higher porosity once the excess water evaporates, and higher porosity results in less attenuation of microwave signals. Part of this effect

is also related to the curing of the samples as a function of less or more free water (i.e., w/c). The J-band (5.85-8.2 GHz) images are also shown in Figure 3-16 where the effect of (w/c) is less noticeable.

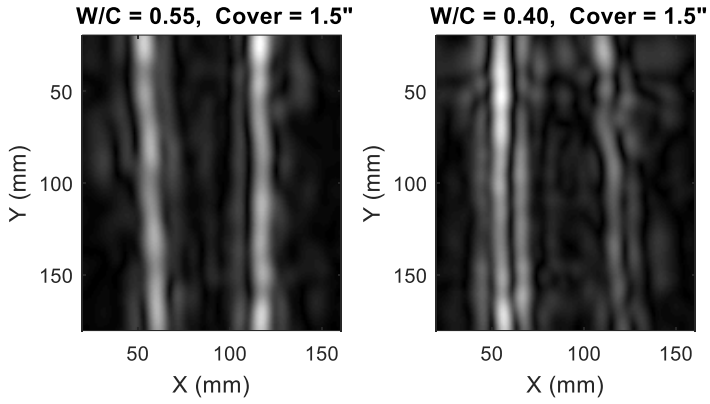

Figure 3-15: X-Band (8.2-12.4 GHz) Images of the blocks with varying water to cement ratio.

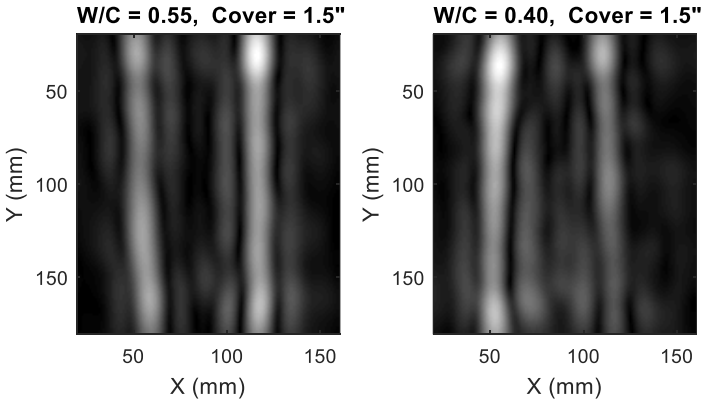

Figure 3-16: J-Band (5.85-8.2 GHz) Images of the blocks with varying water to cement ratio.

3.4.3 Sample group 3

It has been noticed that the corroded samples of group 1 and group 2 may not have undergone the corrosion process properly, which can be reflected the images in Figure 3-15 and Figure 3-16 that the corroded rebar on the right side of each picture are not uniformly displayed. Consequently, a new corrosion process was designed and implemented for creating a more uniform corrosion, as described previously.

Subsequent to the new corrosion process, after the samples were deemed dry, each sample was then scanned at J-Band (5.85-8.2 GHz) and X-Band (8.2-12.4 GHz). Figure 3-17 shows the imaging results for sample 1 for the non-corroded (pristine) state, after one cycle of corrosion, and after two cycles of corrosion, all at J-band (5.85-8.2 GHz). Figure 3-18 shows similar images at X-band (8.2-12.4 GHz). The other three sample showed similar results. Due to its relatively high frequency, X-band (8.2-12.4 GHz) images do not show clear indications of the rebars. On the other hand, J-band (5.85-8.2 GHz) images show clear indications of the rebars. Reason for this is the relationship between penetration depth and the frequency used, as explained earlier. The final images after this cyclical corrosion at J-band (5.85-8.2 GHz) are given in Figure 3-19 and Figure 3-20 for all these four samples. However, the effect of cyclical corrosion is not evident yet. Another issue to be considered is the amplitude level of the rebar indications as shown in the color bars. The expectation is that the amplitude level will remain constant and to be reduced only by the presence of the corrosion. Trends correlating rebar indication amplitude to corrosion progression has not been observed yet on the two outer rebars that are being actively corroded. However, the image amplitude level is changing by as much as 10 times from one scan to the other. We suspect that this is due to inconsistencies in the manner that the samples are being dried. Remaining water in the concrete can increase the permittivity and loss factor of the sample. Also, any remaining slats within the sample can change the permittivity and loss factor as well. The effect of these remaining water and salts on the dielectric properties of the concrete must be estimated to quantitatively estimate the corrosion level.

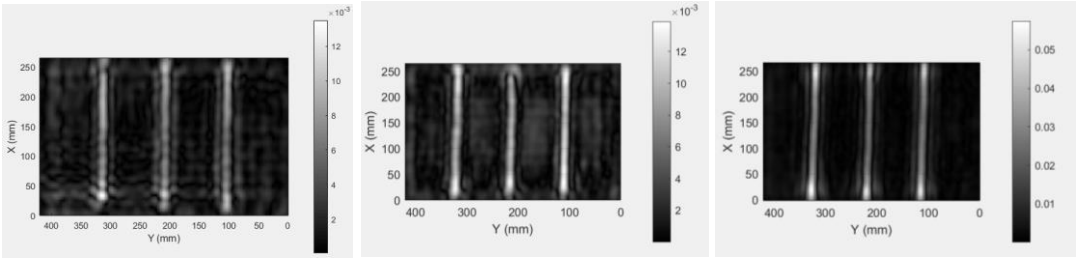

(a) **(b)** **(c)**

Figure 3-17: J-Band (5.85 – 8.2 GHz) SAR images of sample 1 for (a) Cycle 0 (before corrosion), (b) after one cycle of corrosion and (c) after two cycles of corrosion.

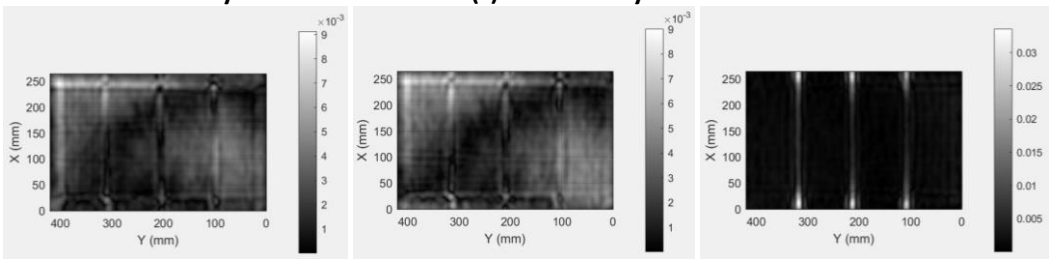

(a) (b) (c)

Figure 3-18: X-Band (8.2 – 12.4 GHz) SAR images of sample 1 for (a) Cycle 0 (before corrosion), (b) after one cycle of corrosion and (c) after two cycles of corrosion.

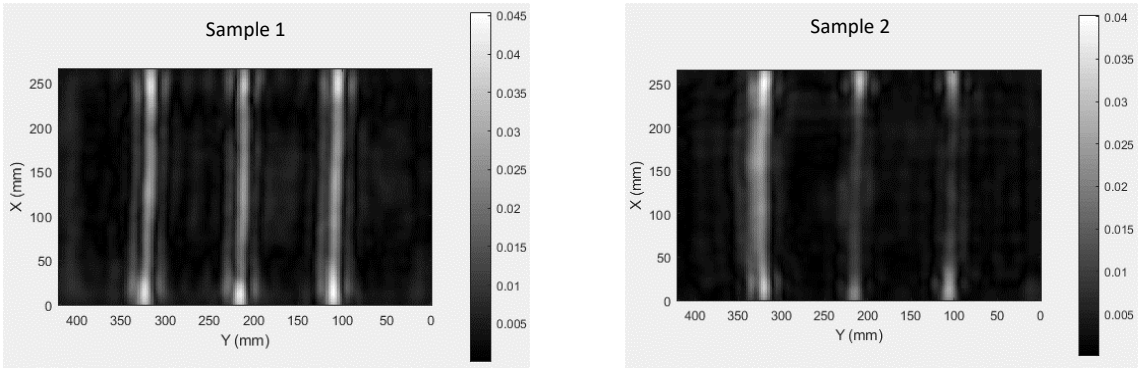

Figure 3-19: J-band (5.85-8.2 GHz) SAR images of samples 1 (left) and sample 2 (right) after 4 cycles of accelerated corrosion.

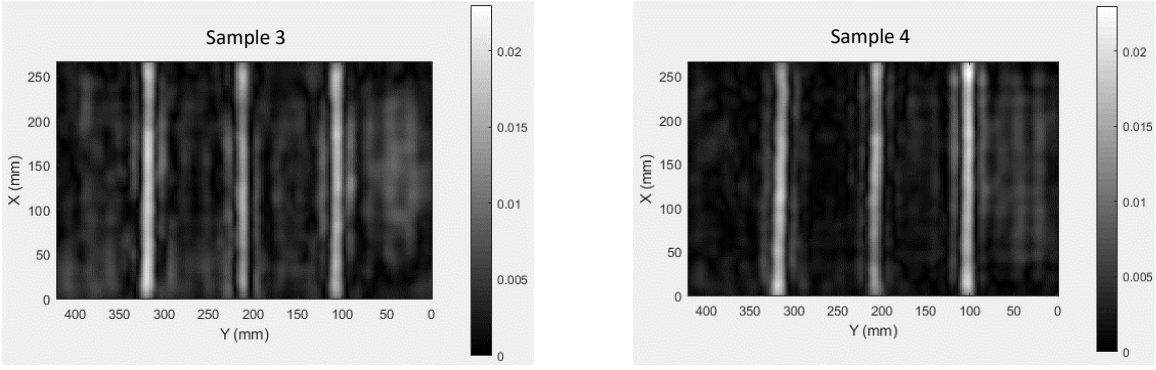

Figure 3-20: J-band (5.85-8.2 GHz) SAR images of samples 3 (left) and sample 4 (right) after 2 cycles of accelerated corrosion.

Due to the *aggressive* accelerated corrosion cycle (soaking and embedding current and then oven drying) the samples cracked along some of the rebars. As such the cyclical corrosion experiment was stopped past the 4th cycle. A final set of imaging experiments were conducted at G-band (3.95-5.85 GHz), J-band (5.85–8.2 GHz) and X-band (8.2-12.4 GHz). Through these measurements and some

corroborating simulations, it was concluded that the effect of corrosion levels on the produced images of rebars was insignificant compared to variabilities in the experiments such as changes in material properties and effect of cracking. In fact, it was shown that cracking contributes to significant level of scattering as shown in Figure 3-21. This leads to SAR imaging being more sensitive for detecting cracking and delaminations (that are more prominent with severe corrosion) than detecting very small levels of corrosion.

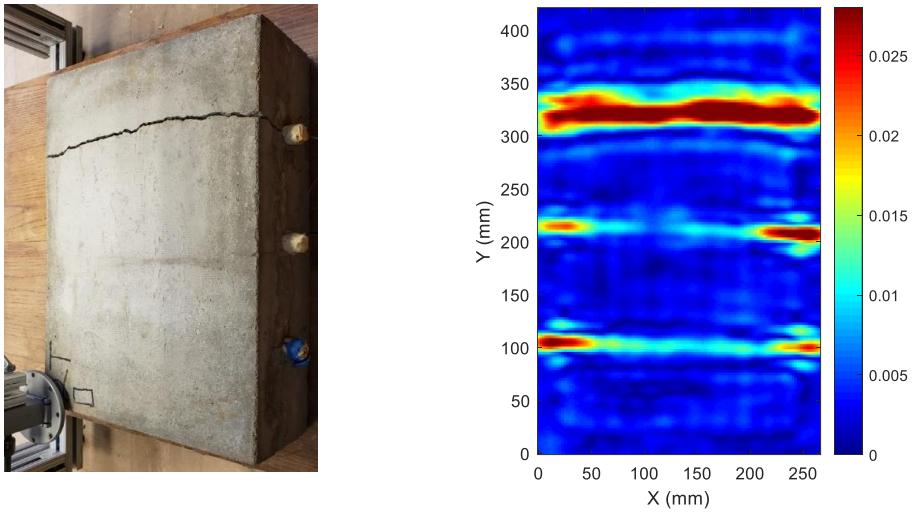

Figure 3-21: Picture of sample 2 being scanned with a J-band (5.85-8.2 GHz) waveguide probe and the resultant SAR image. The image shows a strong indication on the location of the top rebar due to cracking of the concrete.

3.4.4 Rebar in air

Finally, an "air" test specimen containing three rebars similar to the concrete blocks used for cyclical accelerated corrosion was created and is shown in Figure 3-22-left. This specimen also went through cyclical accelerated corrosion and was used to corroborate the simulation results and understand the efficacy of microwave SAR imaging for quantitatively estimating the corrosion level on rebars. This specimen served as a controlled testing platform that removes many unknowns associated with concrete properties. A "control" SAR image of the un-corroded bars at J-band is also shown in Figure 3-22-right.

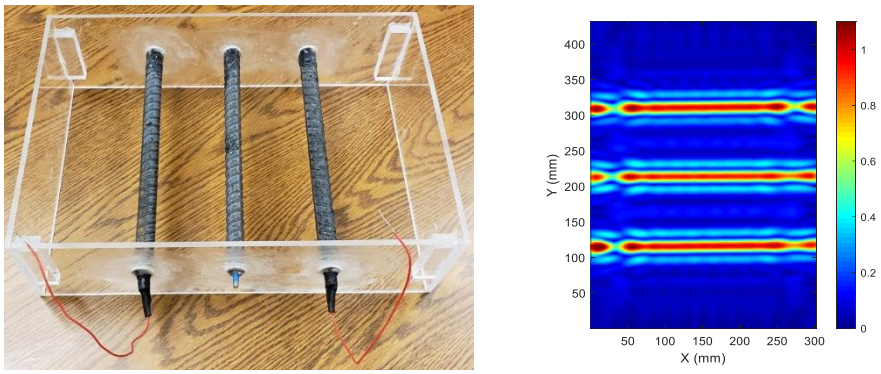

Figure 3-22: Image intensity from the right rebar as a function of increasing corrosion level, experiment setup (left), one of the imaging result (right).

However, when the updated corrosion process was applied , it was found that the corrosion byproduct tends to accumulate at the bottom surface due to gravity. Hence the corrosion distribution is not like what it should be in a rebar and cannot be detected.

3.5 Rebar corrosion simulation for microwave imaging

As mentioned above, both cases when the rebars are embedded into concrete and into air did not quantitatively show the indications regarding the thickness of the cyclical corrosion byproduct. Although in previous experiments this technique has shown to be capable of detecting rebar corrosion [17]. Therefore, simulations were tried to classify the detection limit and hence the sensitivity of a SAR system to the corrosion thickness.

Mn 3.5.1 Sensitivity to corrosion thickness

In this case, electromagnetic simulations were performed by CST Microwave Studio® to investigate the theoretical capabilities of SAR imaging for detecting and assessing corrosion level in rebars embedded in mortar. Figure 3-23 shows the simulation schematic where a plane-wave, at J-band (5.85-8.2 GHz), impinges upon a mortar sample (cross-section shown) with two embedded rebars, one of which (on the right) has varying thicknesses of corrosion on it (discrete 5% increase).

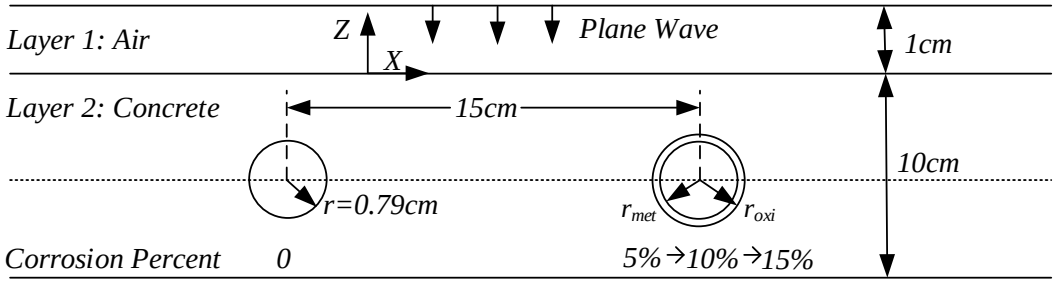

Figure 3-23: Electromagnetic simulation configuration for a mortar sample with embedded rebars.

Specifically, the dielectric constant of the sample was taken to be (ε_r = 4-*j*0.2), while the corrosion (i.e., rust) dielectric constant was taken to be (ε_r = 12.5-*j*2.6). Using CST Microwave Studio®, the reflection coefficient measured at the location of the incident wave (1 cm above the sample) was calculated along the sample (from right to left). This data, representing the measured reflection coefficient, was then passed through the Green's function-based SAR algorithm to produce an image of the cross-section of the sample. The two embedded steel bars are placed at the same depth of 150 cm within the sample, and 15 cm apart, which is large compared with the operating wavelength, to ensure minimal interactions between the two. The thickness of corrosion layer, r_{oxi}, was calculated according to:

$$r_{met} = r\sqrt{1-N_c}\ ,\ r_{oxi} = r\sqrt{1+3N_c} \tag{4}$$

where, r_{met} is the radius of rebar, and N_c is the ratio of corrosion (lost mass of a rebar due to corrosion over its original mass). No corrosion was considered on the left rebar while only the one on the right was corroded as a function of increasing corrosion percentage, N_c, from 0% to 5%, 10% and 15%. The calculated thicknesses are shown in Table 3-2.

Table 3-2: Size of differently-corroded rebars.

Corrosion Percentage	r_{met} (cm)	r_{oxi} (cm)	Thickness (r_{oxi}-r_{met}) (cm)
5%	0.770	0.847	0.077
10%	0.749	0.900	0.151
15%	0.728	0.951	0.223

Figure 3-24a-d show the results of these simulations, in the form of cross-section images of the sample with varying percentage of corrosion. The results clearly show the effect of increasing corrosion level in the (right) rebar image intensities, as a direct result of the lossy nature of the dielectric constant of corrosion/rust. In addition, the results show that the decrease in the image intensity is not a linear function of increasing corrosion level.

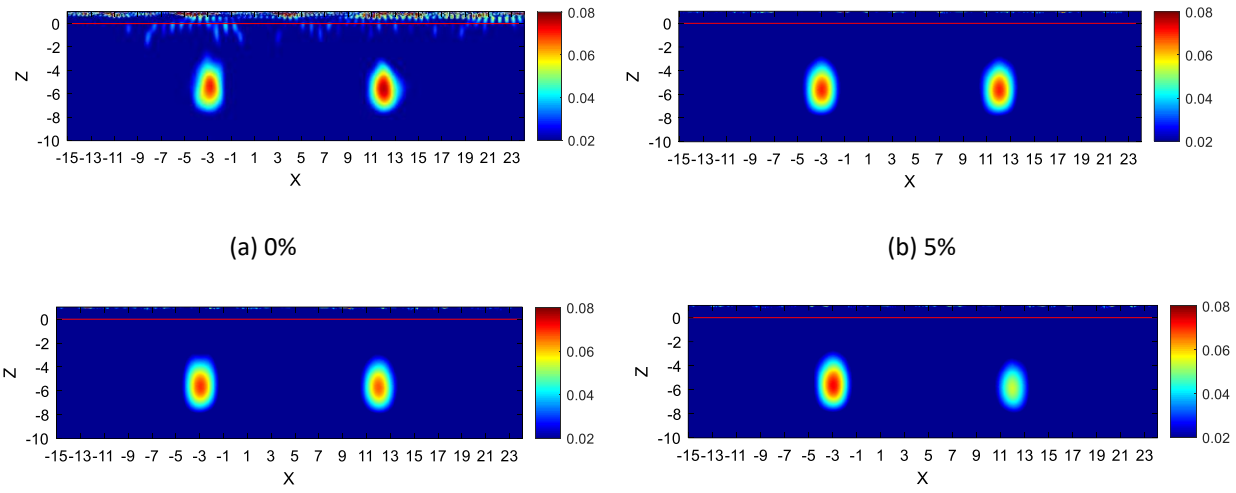

(a) 0%

(b) 5%

(c) 10%

(d) 15%

Figure 3-24: Simulation results for: a) 0%, b) 5%, c) 10% and d) 15% corrosion (N_c), respectively.

To more quantitatively illustrate the effect of increasing corrosion level on the rebar on the right, image intensity magnitude at X = 12 cm, which correspond to the center position of the right rebar in the x-direction (from left to right) is extracted and shown in Figure 3-25. The result shows the gradual, yet non-linear change in the image intensity. More importantly, the non-linear changes of green function in terms of propagation distance [18] leads to the quick decay of signals from 10% case to 15% case while small portion from 0% to 10%.

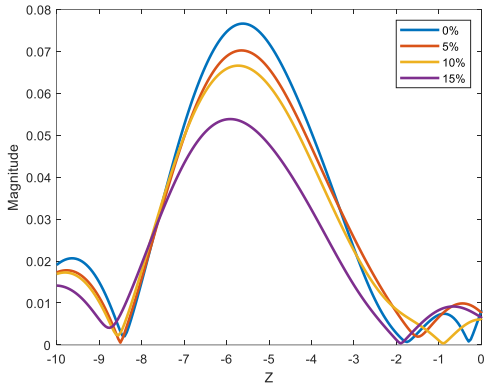

Figure 3-25: Image intensity from the right rebar as a function of increasing corrosion level.

To further explore the detection limit of SAR imaging technique, the corrosion level was changed from 5%-20% to 0.1%-0.4%. The corresponding corrosion thickness with respect to the same rebar used as in Figure 3-23 is given in Table 3-3.

Table 3-3: Thickness calculation of the 0.1%~0.4%-corroded rebars.

Corrosion Percentage	r_{met} (cm)	r_{oxi} (cm)	Thickness (r_{oxi}-r_{met}) (μm)
0.1%	0.7896	0.7912	15.79
0.2%	0.7892	0.7924	31.57
0.4%	0.7884	0.7947	63.07

Using a similar procedure, the final comparisons were made in Figure 3-26. These lines represent the reconstructed reflectivity along the cross-range direction X direction in Figure 3-23) at the depth right across the rebar center (dotted line in Figure 3-23). Since the corrosion byproduct is lossy material, the peak value should be reduced gradually as the thickness of the corrosion byproduct increases. However, as can be seen from Figure 3-26, results both from J-band and X-band do not show any indication about this, leading to the conclusion that SAR imaging technique may not have enough detectability for micrometer-level scale corrosion byproduct.

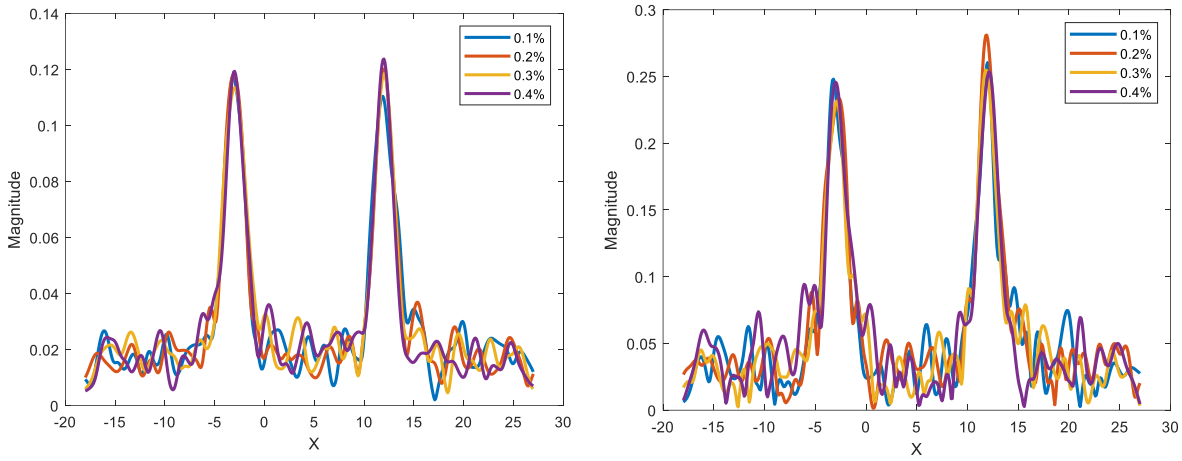

J-Band (5.85-8.2 GHz) X-Band (8.2-12.4 GHz)

Figure 3-26: Simulation results for the setup at different frequency bands

3.6 Resonance simulation for periodically distributed rebars

Another technique that was investigated was the frequency selective surfaces (FSS) approach. In this scenario, the resonant frequency of a structure, which is formed by the periodic copies of the element, is dependent on the geometry and the material of this element and the gap distance between the two neighboring elements. In this case, since the placement of the rebars is usually with fixed gap distance (i.e. ,150 mm), the resonant frequency can be used to detect the geometry and material property changes of the corroded rebar.

3.6.1 Rebar in air

To study this phenomenon and confirm the validity of this idea, full-wave electromagnetic simulations using CST Microwave Studio®, was performed to determine the influence of corrosion on the resonant properties of the overall structure. Figure 3-27-left shows the simulated configuration. Rebars are placed as shown by the right figure. All of them have the same radius 9.525 mm and same distance 150 mm. As shown in Figure 3-27 right, the corrosion layer is also set, the range of which is 0, 0.2%, 0.4%, 0.8%, 1.0%, 2.0%, 4.0%, 8.0%, 10% with respect to rebars' loss of mass. Figure 3-28-left shows results of the magnitude of transmission coefficients (S_{21}) vs. frequency with increasing corrosion

percentage. There is a null in each S_{21} result meaning energy is totally reflected at that resonant frequency. Figure 3-28-right shows the shift of resonant frequency with increasing corrosion percentage. It is clear that even 1% corrosion can theoretically be detected.

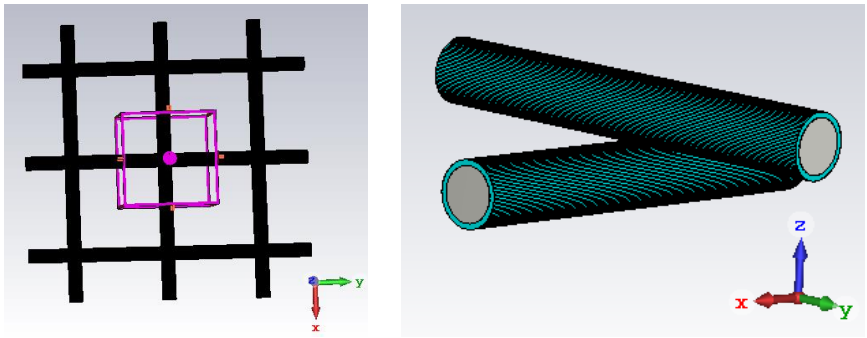

Figure 3-27: Configuration for periodically distributed rebars used in simulation (left), and scene in a junction (right).

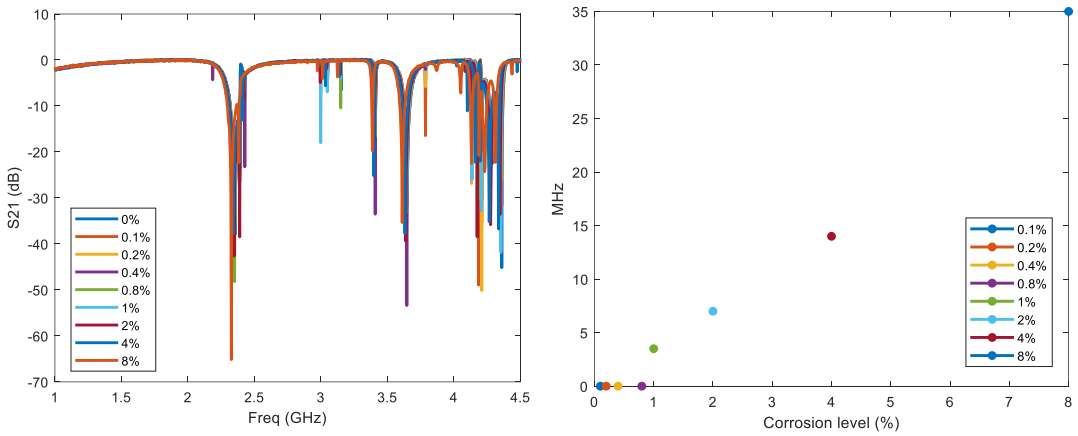

Figure 3-28: results of the magnitude of transmission coefficients vs. frequency with increasing corrosion percentage (left), shift of resonant frequency with increasing corrosion percentage (right).

3.6.2 Rebar embedded in concrete

We have also performed full-wave electromagnetic simulations, using CST Microwave Studio®, of a concrete structure containing periodic (uniformly spaced) rebars. Figure 3-29 shows the CST simulation model where the rebars are along the Y-axis and they are spaced by 120 mm (slightly different from 150 mm but can increase the resonant effect) in the x-axis and the electromagnetic wave is propagating along the Z-axis. Figure 3-30 shows simulated reflection coefficient results as a function of frequency from this model for several different levels of corrosion percentages as used previously. As can be seen

from Figure 3-30, the resonance frequency shifts to the right with increased corrosion level. Figure 3-31 shows a plot of this resonance frequency shift as a function of corrosion level percentage when compared to the no-corrosion case. The results show this method has sensitivity to the corrosion thickness, but not to be sufficiently sensitive to the presence of corrosion.

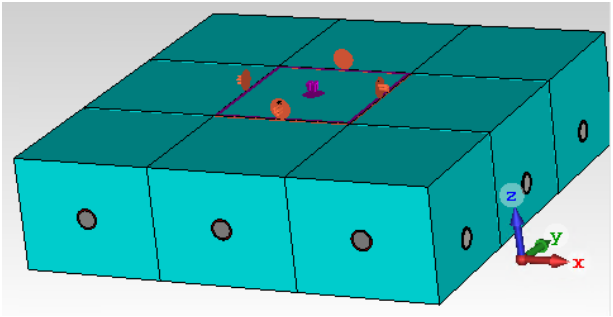

Figure 3-29: CST Microwave Studio simulation model for the periodic rebar structure in concrete.

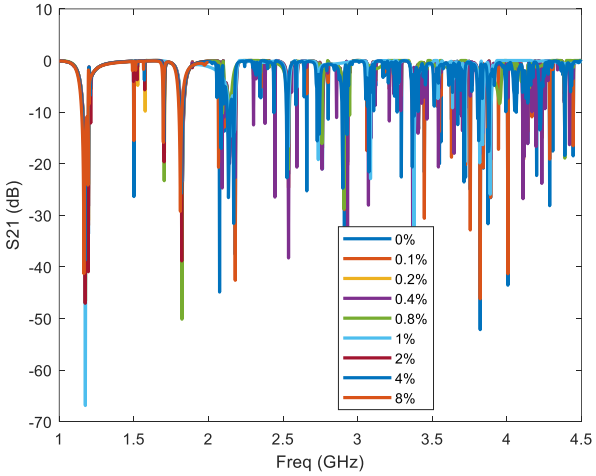

Figure 3-30: Simulated reflection coefficient as a function of frequency for several corrosion percentages.

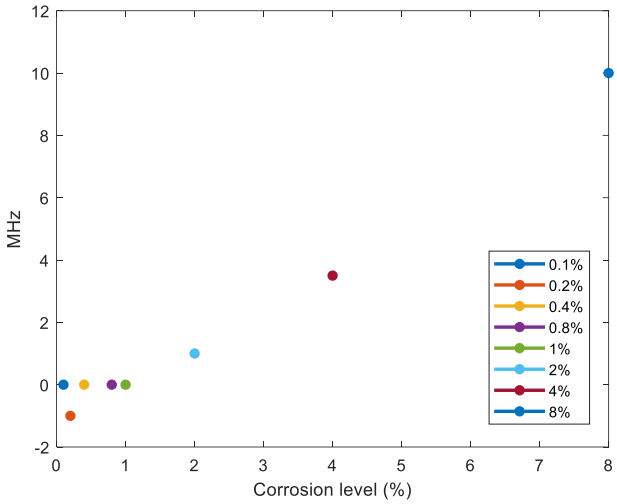

Figure 3-31: Resonance frequency shift as a function of corrosion level percentage.

We also attempted to simulate a more realistic configuration, similar to that as shown in Figure 3-29. The simulation configuration in Figure 3-32 is for eleven rebars embedded in concrete. However, the simulation time was prohibitively time-consuming and was consequently abandoned.

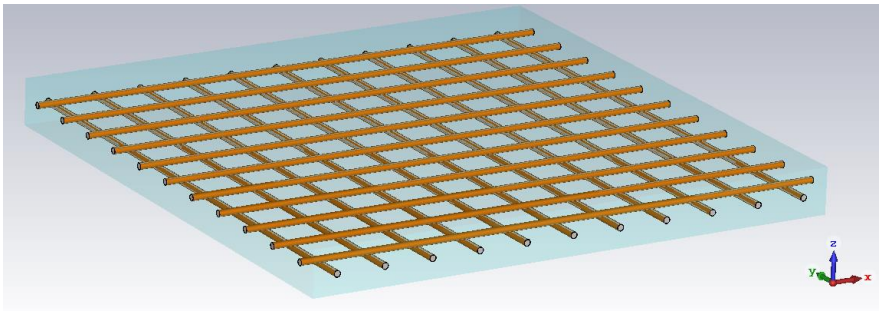

Figure 3-32: More realistic 2D rebar configuration.

3.7 Harmonic measurement on cyclically corroded rebar

We also investigated a method to detect presence (or degree) of corrosion by measuring the power in the generated harmonics from conducting junctions. This testing method relies on the non-linear effects of current flow through junctions (e.g., connections between rebars) that results in harmonics of the interrogating signals being generated. An initial experiment was conducted using the specimen shown in Figure 3-33.

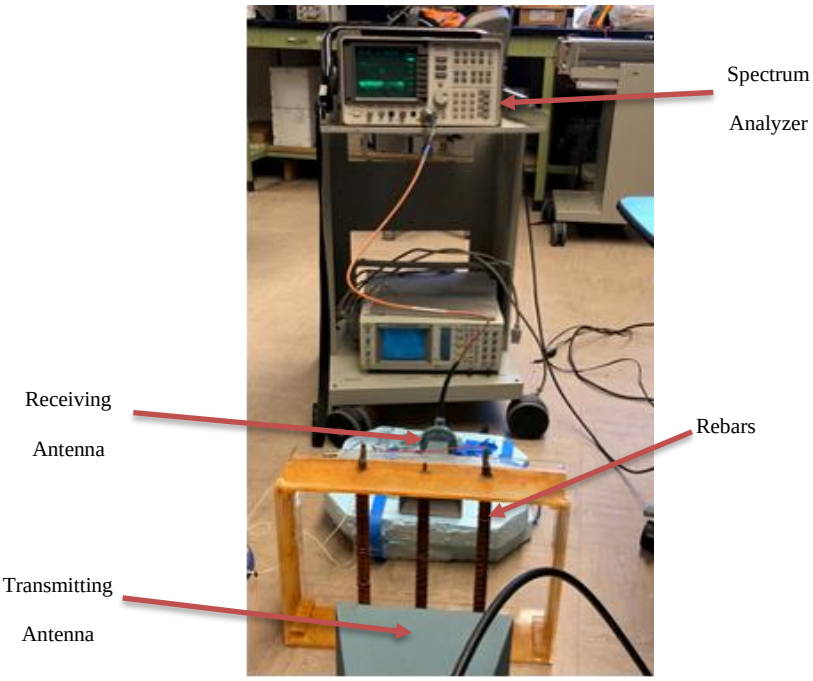

Figure 3-33: Harmonic generation experiment.

A signal source, amplifier and filter (not shown) were used to generate a single tone signal at 2.6 GHz with a power of 1W (30 dBm). The signal was radiated onto a three-rebar sample. The three rebars were electrically connected to each other using wires to create junctions. Due to non-linear effects, harmonics of the incident signals are generated. Specifically, the 3rd harmonic (at 7.8 GHz) is stronger compared to other harmonics. The receiving antenna was chosen such that it receives only the harmonics of the signal which were then measured by a spectrum analyzer. Figure 3-34 shows measurement results, where in the absence of the sample the 3rd harmonic of the signal does not appear since there is no mechanism for generating it. Conversely, in the presence of the sample, the 3rd harmonic has a power of -82.5 dBm.

Noise floor of spectrum analyzer below -110 dBm

Power in the generated 3rd Harmonic from sample -82.5 dBm

Figure 3-34: Initial experiment results for harmonic generation. The left-side image is showing the instrument noise floor, where the 3rd harmonic is not generated without the rebar sample. On the right-side image, the rebar sample generates the 3rd harmonic signal.

To show that the change of corrosion thickness can be detected by this measurement setup, a two-crossed and wrapped rebars was built as shown by Figure 3-35 (left) and Figure 3-36 (left). These two rebars were cyclically corroded from 0 hours to 96 hours. Figure 3-35 (right) shows the result by 24-hours corrosion and Figure 3-36 (right) shows the result by 96-hours corrosion. The longer time of corrosion, the lower peak value of 3rd-order harmonic.

Figure 3-35: Configuration of rebars after 24-hours corrosion (left) and the measured 3rd-order harmonic (right).

Figure 3-36: Configuration of rebars after 96-hours corrosion (left) and the measured 3rd-order harmonic (right).

After 96-hours of corroding the rebars, we also gradually removed the corrosion on the junction of this two rebars by brushing some of corrosions away in each round. Figure 3-37 shows magnitude of 3rd-order harmonic vs. amount of corrosion. It confirms that the less corrosion on this junction, the higher peak value.

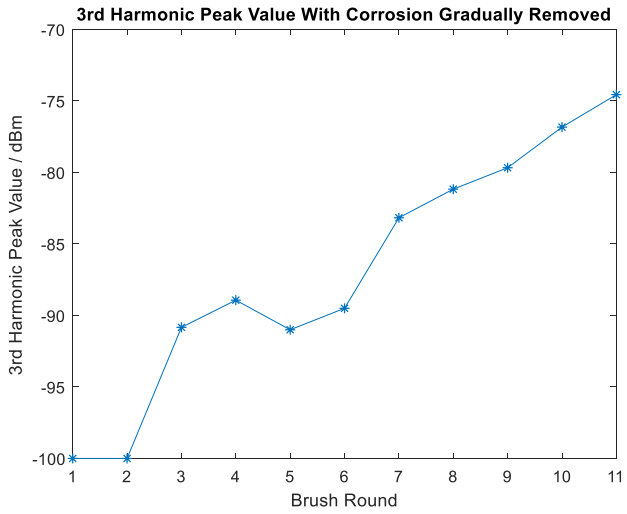

Figure 3-37: The increase of 3rd-order harmonic's magnitude by gradually brushing corrosion away.

3.8 Bridge delamination detection

A pedestrian bridge on campus (between ERL and Computer Science buildings of Missouri S&T) which shows visual signs of rebar corrosion and delamination, was imaged with the permission of university officials.

For this purpose and as a way of preparing for this investigation, a new imaging system to collect and process the data is needed. Due to the size of the pedestrian bridge, data collection had to be conducted manually. Consequently, several tests in the lab were conducted first to get prepared for the in-field tests on the bridge. Figure 3-38 shows the setup and the produced image of a rebar. As can be seen from it, the rebar can be clearly indicated even though embedded in the foam sheets.

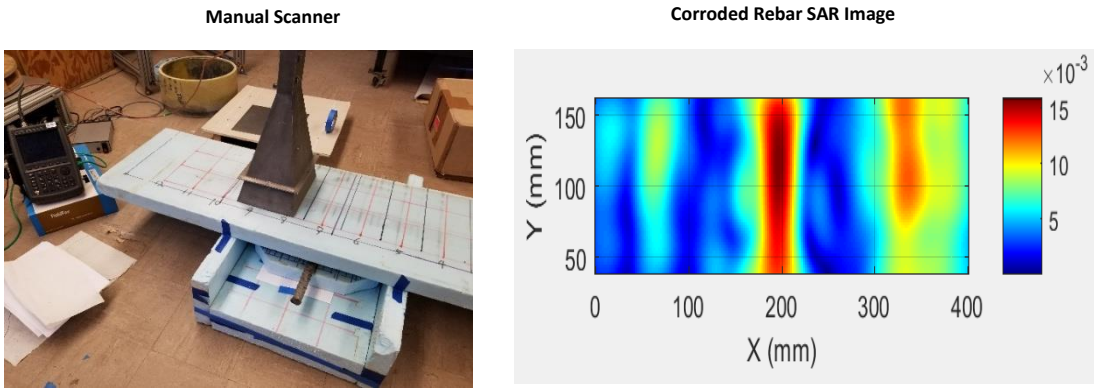

Figure 3-38: Manual Scanner setup for corroded rebar (left) and processed results from SAR imagining (right).

Then, same method was used to scan the bridge. In this case, the top portion of this bridge (the computer science pedestrian bridge) was manually scanned in four sections using a wideband horn antenna operating in the 1 – 4 GHz frequency range. Figure 3-39-top shows the scanned sections from A-D along with the SAR imaging results (Figure 3-39-bottom). As can be seen from it, some highlight points are displayed which may be the indications about delamination.

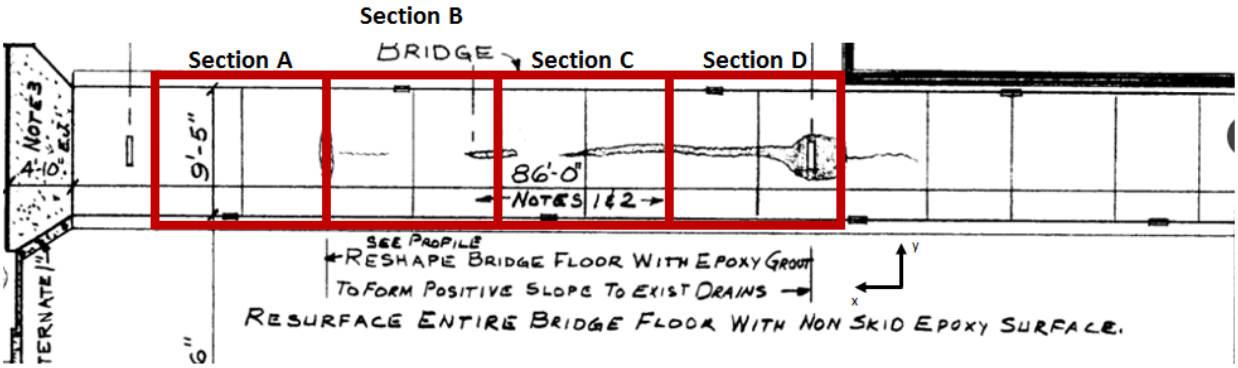

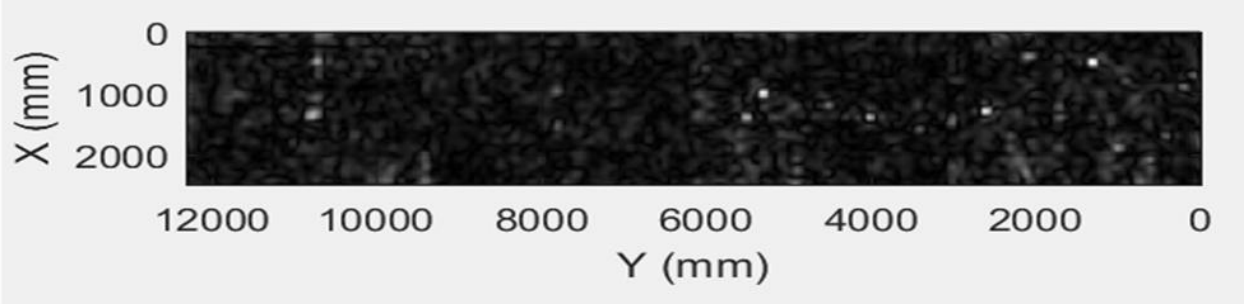

Figure 3-39: Target sections that were scanned (top) along with the results of the entire bridge (bottom)

To make clearer indications about delamination, it was found that the aforementioned deterioration effects (as shown in Figure 3-40 and Figure 3-41-top) of the middle section of this bridge can be visually observed. In this case, both the top side and bottom side were imaged by conducting manually scanning using a wideband horn antenna connected to a field-portable vector network analyzer (VNA) operating in the frequency band of 1 to 4 GHz. These measurements were conducted on a 2D measurement grid with spacing of 10 cm. The antenna, which had an aperture of ~230 mm x 180 mm (same as before), was manually moved across this grid. The collected data were then processed using the SAR algorithm to form 3D images. Two-dimensional (2D) Image slices at depths of interest were then produced.

For the scanning from the top side, Figure 3-40 shows the sliced image at a depth of ~80 mm inside the concrete. Due to the repair and resurfacing work the exact depth of the first rebar layer cannot be ascertained. But the image in Figure 3-40 shows indications in multiple areas of the bridge. These can be due to delamination (mainly as a result of rebar corrosion) or features in the bridge deck from the repair work conducted in the past.

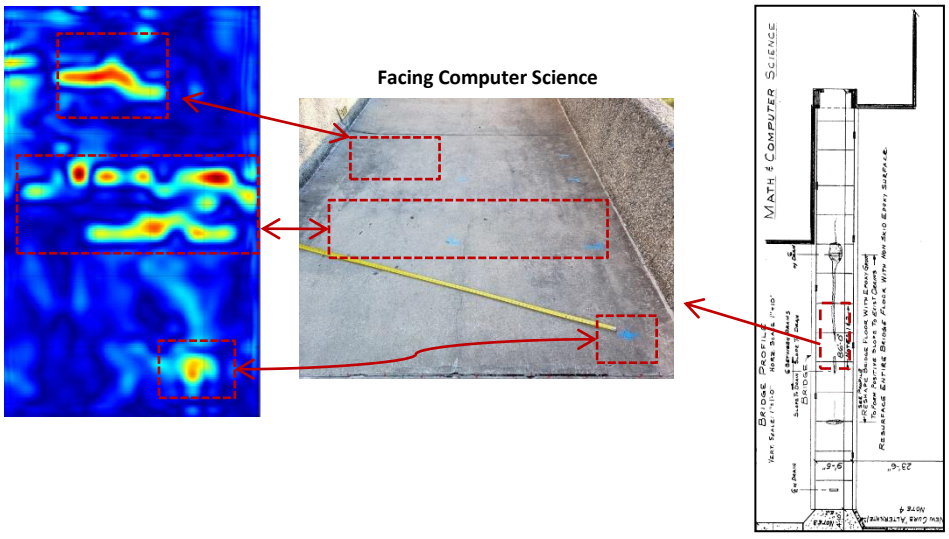

Figure 3-40: SAR image of a section of the topside of the bridge.

For the scanning from the bottom side, Figure 3-41 shows the image produced in a same way as above from the under-side of the bridge and focused at a depth of 40 mm inside the concrete (closely corresponding to the location of rebars). This image shows the delamination which is more severe near the edge of the bridge, as also is visible from the outside, as well as its extent and spread towards the middle section of the bridge. Also visible in this image are indications near X = 500 mm, one which corresponds to a location in the concrete with signs of deterioration and another which does not correspond to any visible feature on the outside of the bridge. This latter indication may correspond to a void, pocket of high moisture, or an unknown embedded structure (e.g., drainage pipe) inside the bridge. This may be probably confirmed with additional testing or better yet with destructive testing.

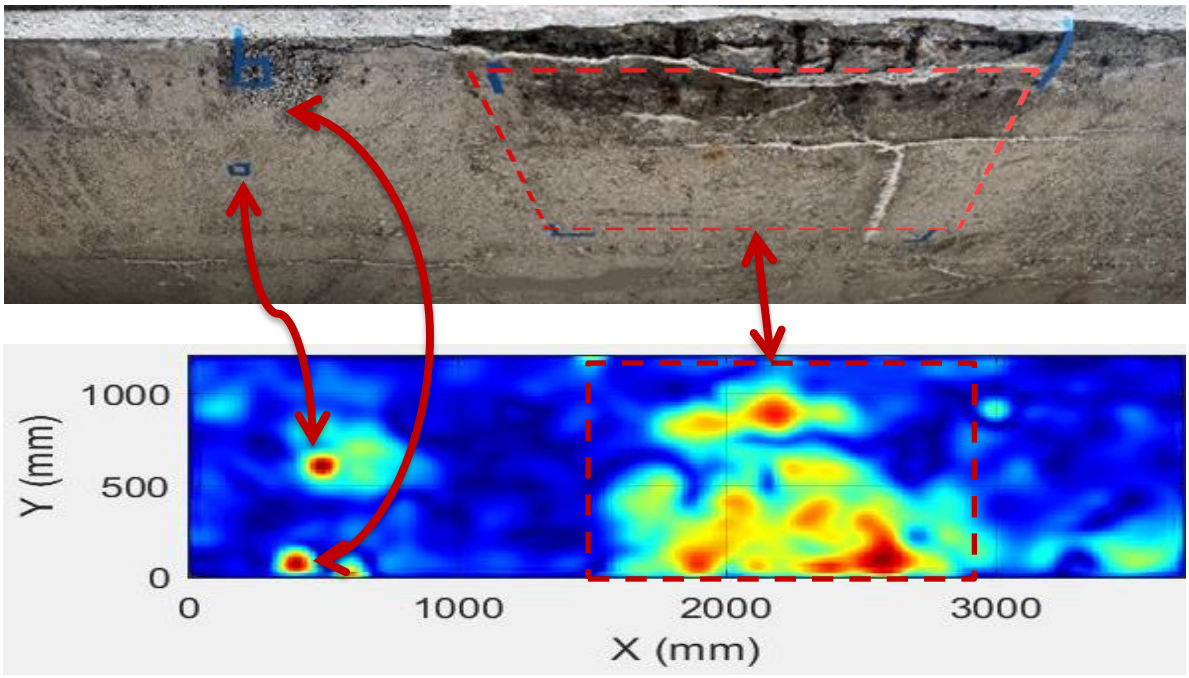

Figure 3-41: SAR image of bridge underside with indications corresponding to visible as well as non-visible damage in the bridge.

3.9 Simulated delamination detection

In this section, the detectability of SAR system to the delamination embedded into concrete is investigated. A large concrete block with simulated delamination was cast as a platform to do experiments, and the corresponding results from several experiments are discussed and analyzed. Associated scanning components such as antennas were also developed and are introduced as well.

3.9.1 Concrete casting with delamination

Firstly, A large 6' x 4' concrete slab containing simulated delamination and voids was cast, as shown in Figure 3-42 and Figure 3-43. The concrete slab was 8" thick and contained two-levels of rebar grids with spacing of 6" on the left side of the sample and 12" on the right side of the sample as indicated by the red lines in Figure 3-42. Foam blocks were used to create voids and thin plastic sheets were used to create delamination with different sizes and locations as shown in Figure 3-42 below. Figure 3-43 shows

pictures of this sample before and after casting the sample. This sample has been imaged several times to evaluate the capabilities of SAR imaging for detecting delamination in concrete.

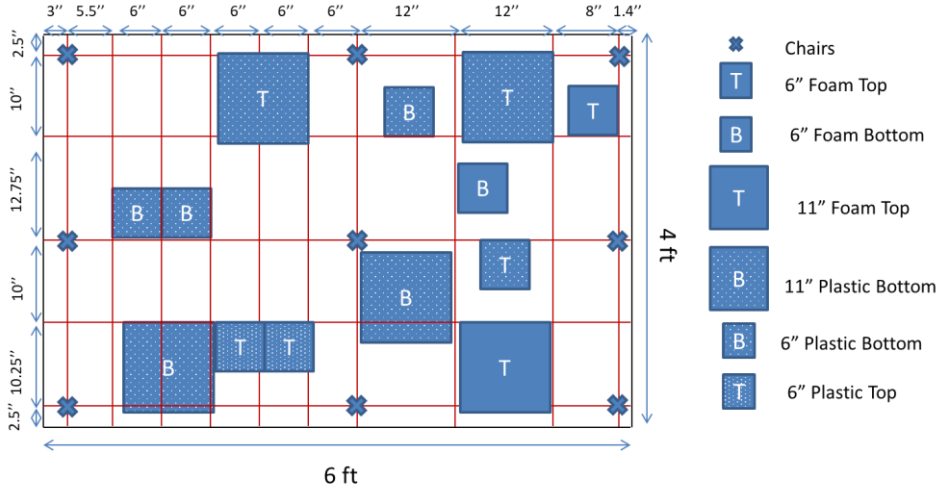

Figure 3-42: Schematic of the delamination sample.

Figure 3-43: Pictures of the delamination sample before and after concrete pour.

3.9.2 Antennas for scanning

It has been verified that antenna is one of the key components in a SAR imaging system, and the properties of the antenna used play a significant role in the final image quality. In this case, as discussed in section 2.1, the antenna used should be wideband, has lower starting frequency. To this end, two antennas, which are Vivaldi antenna and double-ridged TEM horn attached with curved surface, were designed and fabricated.

3.9.2.1 Vivaldi Antenna

As a frequency-independent antenna, Vivaldi antenna is naturally wideband. Hence, it is a good potential candidate for antenna used for wideband SAR imaging. To this end, antipodal Vivaldi antenna, one of the popular antenna designs, was designed by using CST Microwave Studio® simulations.

The geometry of this antenna is shown in Figure 3-44. It operates in the frequency range of ~0.8 – 5 GHz. The size of the antenna is about 220 mm (length) and 220 mm (width). To reduce the lower starting frequency, corrugations were applied to the side edges as shown in Figure 3-45 to increase the propagation path of the induced surface currents. In this case, the new operating frequency range is from 0.5GHz~4GHz as shown by S11 in Figure 3-46 with only slight extrusions above -10 dB around 1GHz~1.3GHz. This low-frequency and wideband antenna can bring us deeper penetration depth.

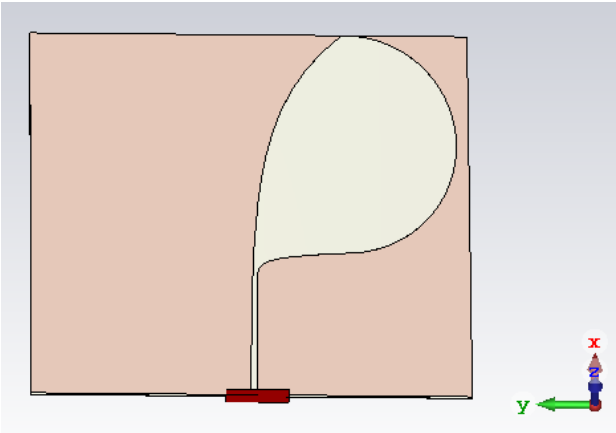

Figure 3-44: CST Microwave Studio model of a Vivaldi antenna.

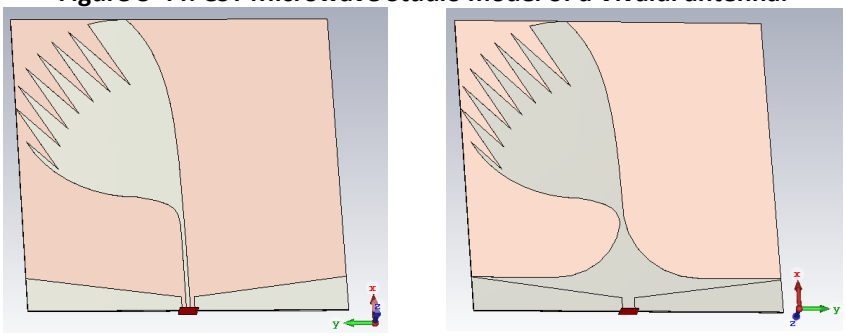

Figure 3-45: Top side (left) and back side (right) of Vivaldi antenna.

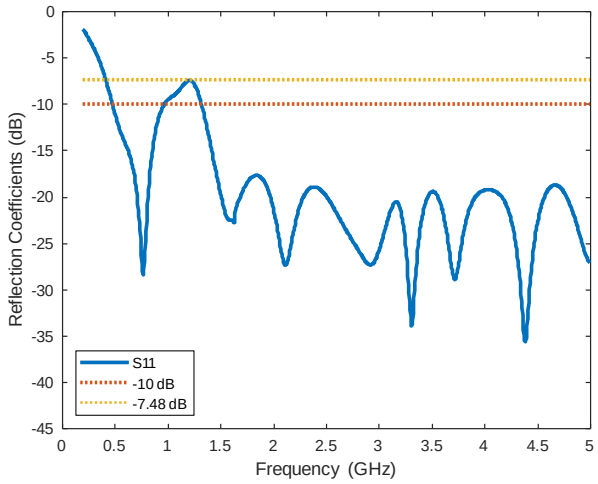

Figure 3-46: Reflection coefficient (S11) of Vivaldi antenna.

Meanwhile, a good compromise is also obtained between the beamwidth and gain. As discussed previously, wide beamwidth results in higher resolution, but it means lower gain as well leading to lower signal-to-noise ratio. In this case, as can be seen from Figure 3-47, which displays the far-field gain pattern of this antenna at 2 GHz, the gain is about 6.5 dB while the beamwidth is more than 100 degree in the E plane.

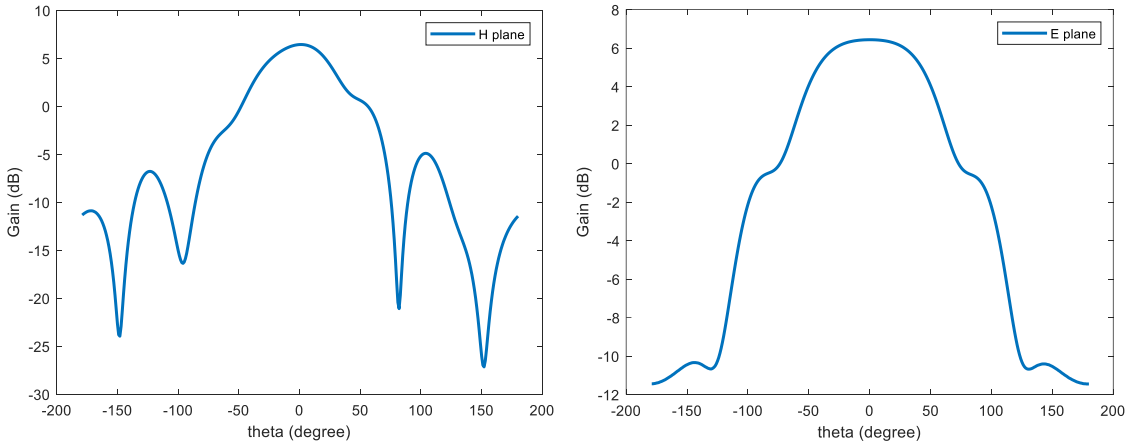

Figure 3-47: Radiation pattern of Vivaldi antenna at 2GHz.

To this end, this antipodal Vivaldi antenna was fabricated, and its reflection coefficient was measured. As expected, the results showed that this Vivaldi antenna has wider frequency bandwidth and lower low-cutoff frequency which can bring higher resolution and larger penetration depth. Figure 3-48 (left)

shows the fabricated physical antenna and Figure 3-48 (middle) shows the measurement setup. In this measurement, Vivaldi antenna is connected to the VNA (vector network analyzer) and is placed into the center of a chamber. This chamber is used to absorb electromagnetic waves so that none of these waves transmitted by the Vivaldi antenna will be reflected. In this case, only reflections from the internal structure of the antenna are considered. Figure 3-48 (right) shows that the S11 is smaller than -10 dB with frequency ranging from 0.5GHz to 5GHz though with a slight deficiency around 1-1.3GHz.

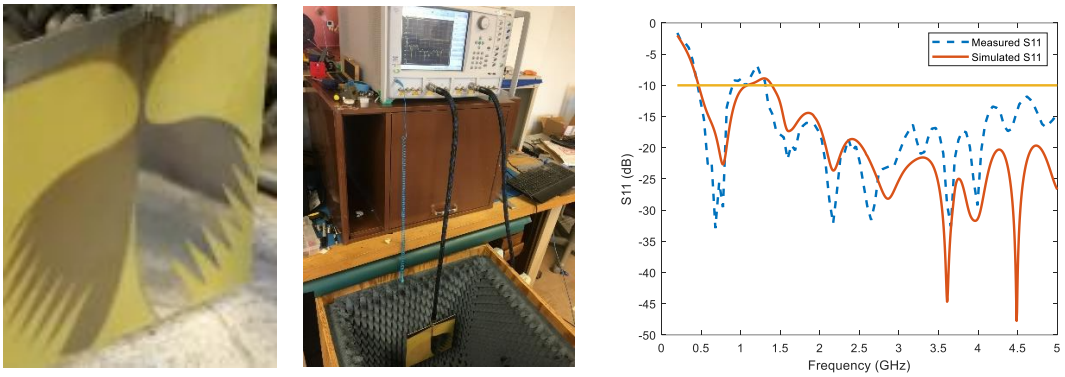

Figure 3-48: Fabricated Vivaldi Antenna (left), reflection coefficient setup (middle), and results of measured and simulated reflection coefficients (S11, right)

Meanwhile, a design about an adaptive imaging array was also conducted based on the above Vivaldi antenna. In this case, as can be seen from Figure 3-49, the antennas are spaced by the ideal sampling distance of quarter-wavelength (λ/4) at the highest frequency (i.e., λ/4 = 15 mm at 5 GHz). This 15 mm physical distance is 10 times the quarter-wavelength distance at 0.5 GHz which means that the antenna at 0.5 GHz can be 10 times larger. Alternatively, 10 of the original Vivaldi antennas can be used to synthesize a larger (and hence more efficient) antenna for transmitting the 0.5 GHz signal, as illustrated in Figure 3-49. Similarly, 5 antennas can be used for 1 GHz and so forth. Figure 3-50 shows how the gain can be increased (in particular at lower frequencies) when a number of antennas are designed to operate as one antenna. It must be noted that the gain also increases at higher frequencies. Further simulations will be conducted to fully test the efficacy of the design.

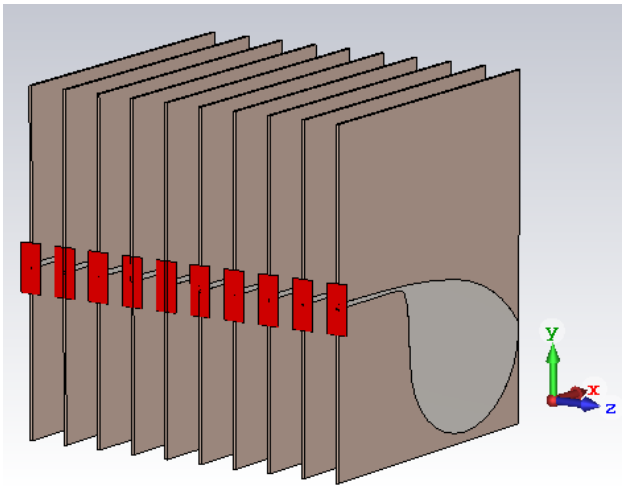

Figure 3-49: Simulation model for using 10 antennas to synthesize a more efficient antenna for lower frequencies.

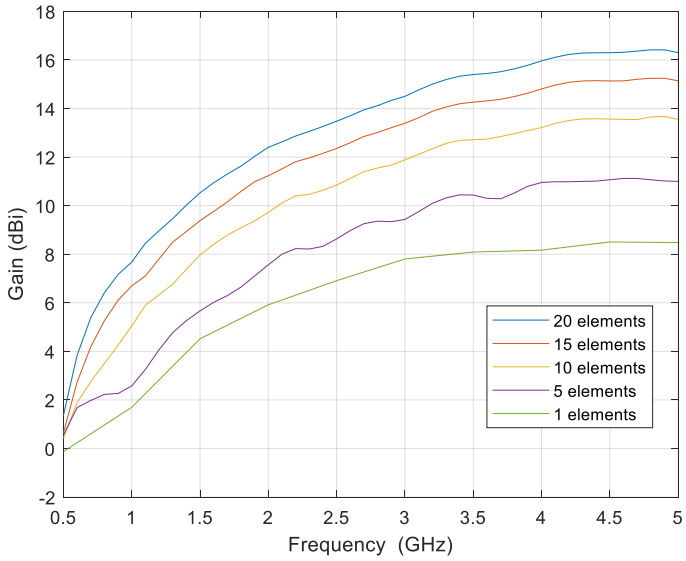

Figure 3-50: Antennas gain as a function of frequency for different number of antennas operating as one antenna.

3.9.2.2 Curved horn

Even though the above Vivaldi antenna can provide low starting frequency, its gain is not high enough at that low starting frequency end (0 dB). In this case, to improve the penetration depth, an antenna with higher gain, and also lower starting frequency at the same time is highly desired.

To this end, it was found that horn antenna can provide high gain, and structure like ridges and curved launch surfaces can be used to reduce the low starting frequency. Therefore, a double-ridged waveguide horn antenna was designed to provide higher gain, larger frequency bandwidth and smaller lower cutoff frequency. The structure of the ridged antenna is given in Figure 3-51-left, which mainly includes three parts: coaxial feed, coaxial-to-waveguide transition, and the horn section.

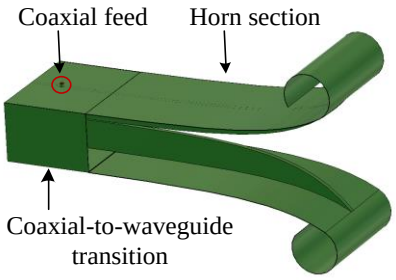

Figure 3-51: Three-dimensional view of the Vivaldi antenna.

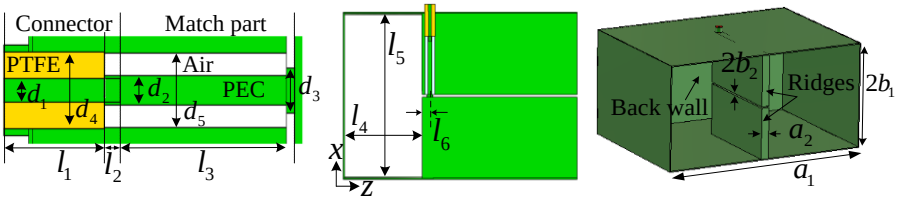

Figure 3-52: Structure of the coaxial feed (left), cross-section view (middle) and 3D view (right) and of the coaxial-to-waveguide transition.

Specifically, for the coaxial feed, it was found that currently available commercial connectors do not have sufficiently long central pin to go through the entire ridged waveguide section height (the length of b_1 in Figure 3-52-right). Consequently, a matched air-filled coaxial line was designed to extend the reach of the N-type connector used. The dimensions of this section are optimized by considering impedance matching between the connector and the ridged waveguide. The entire structure of the coaxial feed is shown in Figure 3-52-left, in which areas covered by green, yellow, and white colors represent the antennas metallic structure which is modelled as a perfect electric conductor (PEC in simulation),

dielectric material (PTFE) filling the N-connector, and air, respectively. The optimized dimensions for this structure can be found in Table 3-4.

Table 3-4: Dimension of the proposed antenna (Unit: mm).

Para.	Value	Para.	Value	Para.	Value
a_1	120.5	d_3	2.4	l_4	30.5
a_2	4.5	d_4	4.1	l_5	62
b_1	31	d_5	3.96	l_6	3.05
b_2	0.5	l_1	12.1	l_7	60
d_1	1.27	l_2	1.9	l_8	260
d_2	1.58	l_3	20	l_9	140

Then, for the coaxial-to-waveguide transition, it is known that at transition point from the coaxial feed to the ridged waveguide, the waves travel in two directions: forward (+z) and backward (-z), as shown in Figure 3-52-middle. A back-cavity is designed with approximately $\lambda_c/4$ length (l_4), where λ_c is the wavelength of the center frequency, such that the backward propagating wave encounters an open-circuit line ensuring that the back-propagating wave reflects back and propagates forward in-phase with the forward propagating wave. The very high impedance of the back-cavity is in parallel with the impedance of the ridged waveguide, therefore the impedance seen from the coaxial feed is close to the impedance of the ridged waveguide. This impedance matching allows for minimizing the reflections seen by the wave in the coaxial feed and transitioning to the ridged waveguide.

For the horn section, it can be seen that two circular surfaces are attached at the end of the two flares, for better impedance matching. The two attached 3/4-circle surfaces play an important role in reducing the lower operating frequency. In this case, the impact of the curvature radius r is investigated and the simulated (using CST Microwave Studio®) results are shown in Figure 3-53. As can be seen from it, , as r increases, the smallest lower operating frequency of 0.5 GHz can be obtained for r=25 mm. Figure 3-53-b shows that the magnitude and beamwidth (57, 60, 66, 77, 66 degree from r=5 to 45 mm) of the radiated field distribution at 0.5 GHz (selected at a specific distance of 180 mm) both increase

until r=25 mm. The field distribution at 2 GHz at the same depth is shown in Figure 3-53-c. The results show that, with r increasing, the half-power beamwidth (HPBW) increases first and then decreases. The optimum radius r is selected to be 25 mm. The final optimized antenna parameters are given in Table 3-4 as well.

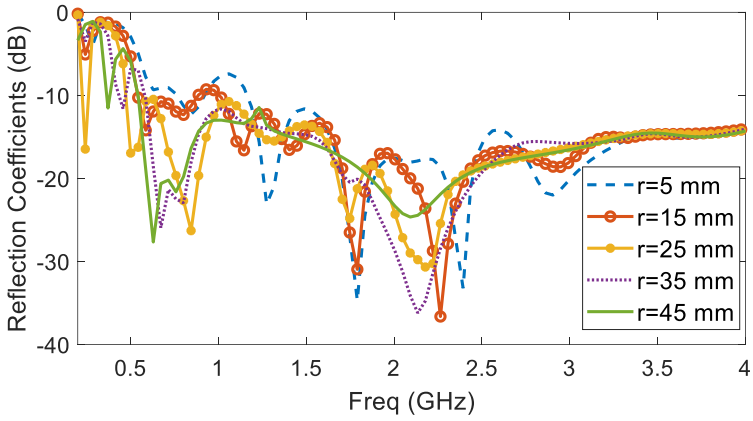

(a) reflection coefficient.

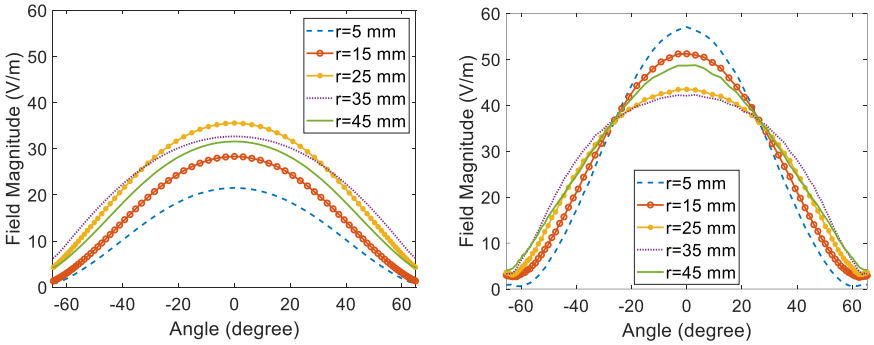

(b) field distribution at 0.5 GHz. **(c) field distribution at 2 GHz.**

Figure 3-53: Simulated results for evaluating the influence of the radius of the curved surface.

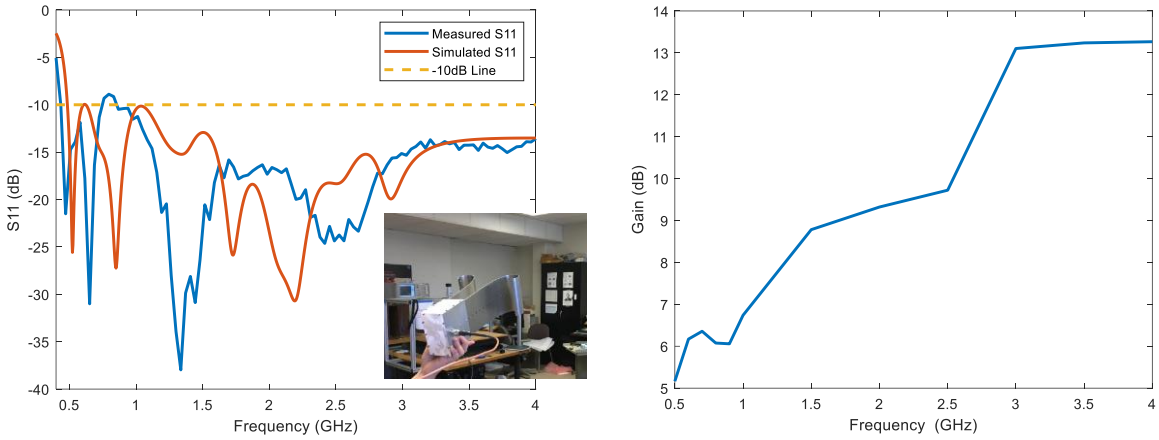

Figure 3-54: Results of S11 from simulation and measurement (left), gain (right)

Both the fabricated antenna and the setup for measuring reflection coefficients are shown in Figure 3-54 (left). The fabricated antenna is connected to a vector network analyzer (VNA), while radiating into free-space to minimize unwanted reflections. Measured reflection coefficient results are shown in Figure 3-54 (left), in which the lower operating frequency is a bit smaller than the simulated expectations. The results do not match well around 0.7-0.8 GHz due to fabrication inaccuracies. The gain of the antenna is also obtained from simulation, which is given in Figure 3-54-right, which shows that at 0.5 GHz, it has 5 dB gain which is much larger than that of Vivaldi antenna. The radiation pattern at 1 GHz is also shown in Figure 3-55 as a reference.

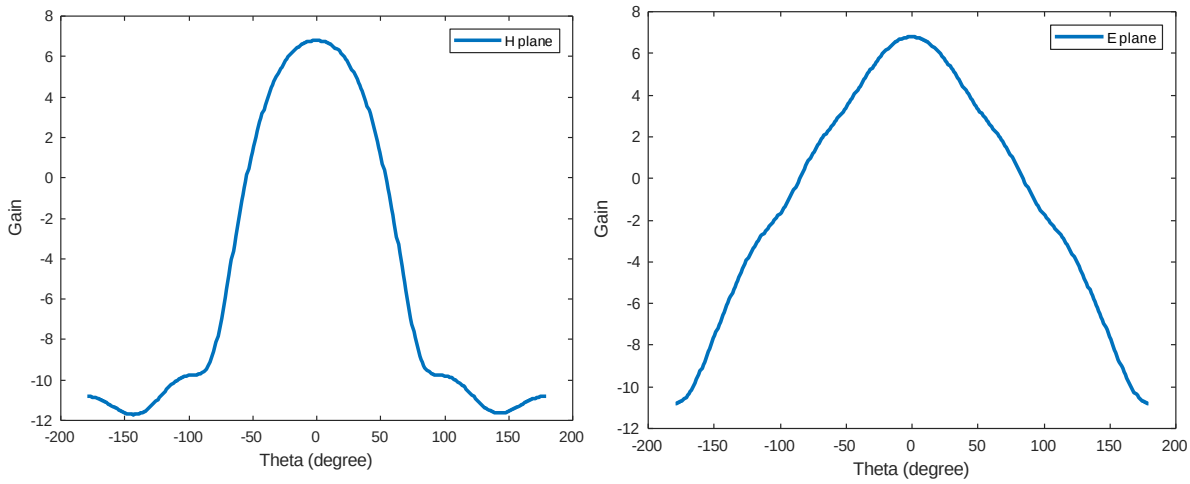

Figure 3-55: Far field pattern of double-ridged waveguide horn antenna, H plane (left) and E plane (right)

3.9.3 Imaging results and analysis

The above designed antennas were used to do scanning over the above-mentioned large concrete block. In this case, as a reference, S-band waveguide and another pyramidal horn (operating from 1-4 GHz) were used to do scanning as well.

3.9.3.1 Imaging results

In this case, the measured reflection coefficients were processed by SAR algorithm and produced SAR images are given in Figure 3-56 at a depth of 100 mm with respect to the concrete surface. As can be seen from the four figures, the rebars can be clearly detected by pyramidal horn antenna while the shape of the big foam, the existence of the plastic can be indicated by curved horn and Vivaldi antenna. S-band waveguide can indicate the existence of foam, plastic and rebars, but not clear.

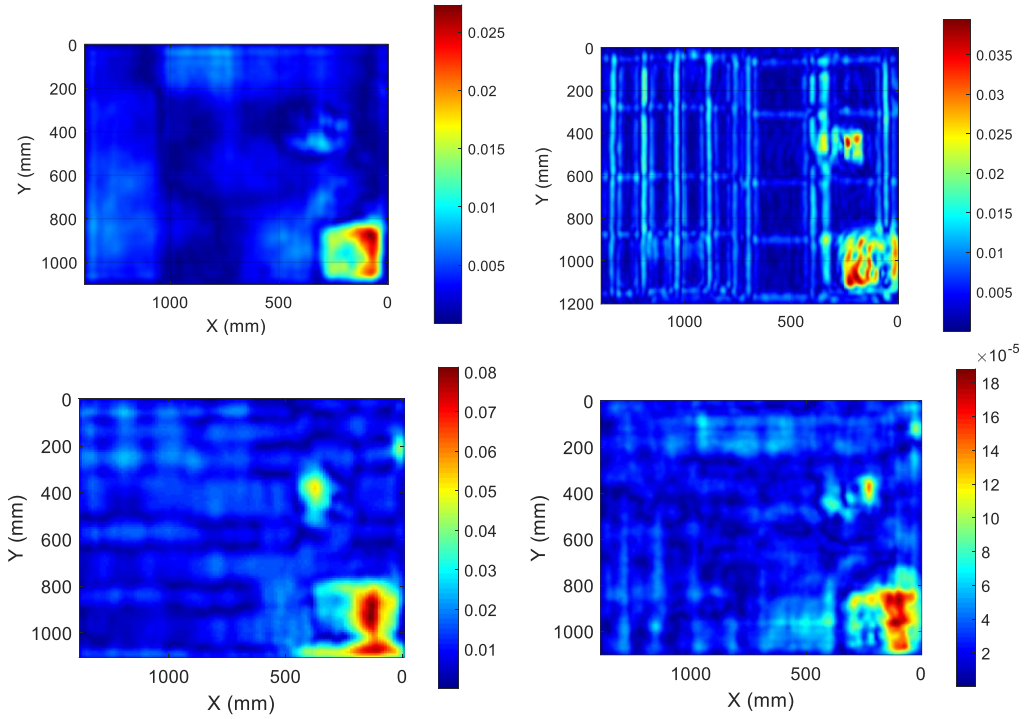

Figure 3-56: Images from SAR processing obtained by curved horn antenna (upper left), pyramidal horn (upper right), S-band waveguide (bottom left), Vivaldi antenna (bottom right)

3.9.3.2 Analysis

In order to analyze the difference in the above four images towards the features of the antennas used, the operating frequency range and the peak gain as a function of frequency are given in Fig. 3-57 left and right, respectively. As can be seen from it, S-band waveguide has smaller frequency bandwidth, ranging from 2.6 GHz to 3.95 GHz, so resolution of its image is not as good as other three at 100mm depth. The diameter of rebar is electrically small compared with wavelength resulting in the very small value of electric field around it. Pyramidal horn antenna has the highest gain and hence much stronger signal from rebar can be received by it.

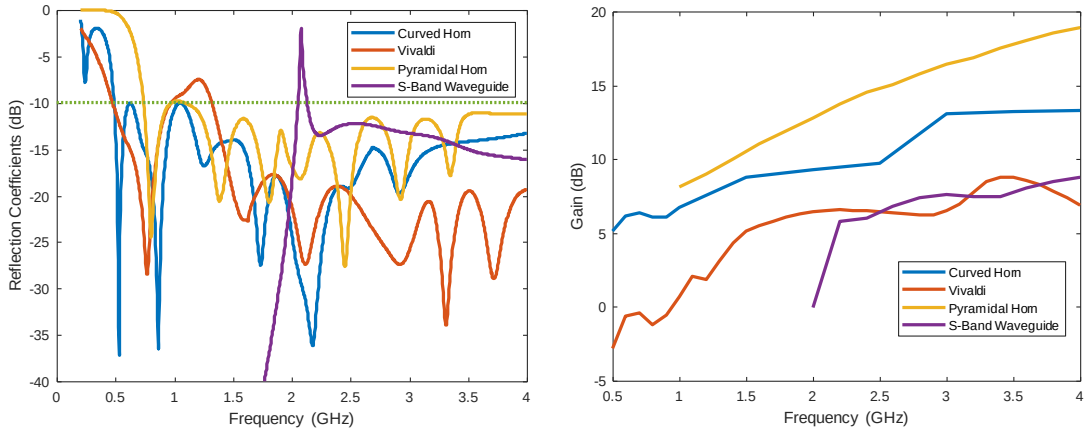

(a) (b)

Fig. 3-57: Simulated: (a) reflection coefficient, and (b) gain of the three antennas.

For the detectability of the plastic and foam sheets, the beamwidth among them were examined. In this case, the field distributions of all the antennas used were simulated given that a large concrete block is placed in front of these antennas with 10 mm standoff distance, as shown in Figure 3-58. The permittivity used for the concrete is 4-*j*0.2. Moreover, the depth used to plot the electric field is at 120 mm with respect to antenna aperture plane. Considering that the center frequency used here is around 2.5 GHz with 120 mm wavelength and the permittivity of concrete is 4-j0.2 resulting in 60 mm (~$1/\sqrt{\varepsilon}$) wavelength (λ) in concrete. Therefore, the depth distance is about 2 λ which is a common case in NDE problems and also roughly the position of the plastic sheets and foam sheets placed.

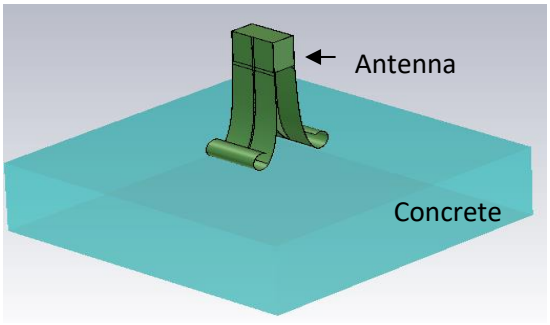

Figure 3-58: Field distribution Simulation setup for different antennas illuminating a big concrete block with 10-mm standoff distance

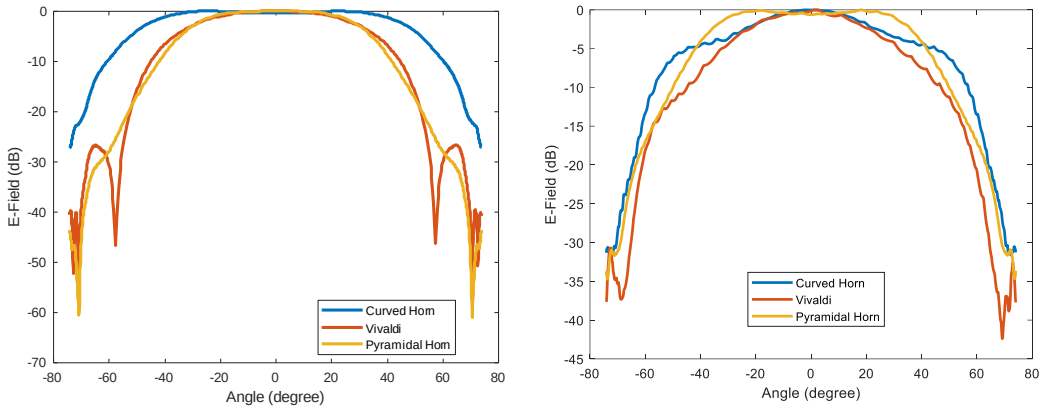

Figure 3-59: Electric field distributions of the three antennas at 2.5 GHz: H-plane (left), and E-plane (right).

To remove the different calibration errors among these antennas, narrow band simulation results at 2.5 GHz are shown in Figure 3-59, which shows that the electric field distributions are plotted as a function of position for both E-plane and H-plane. In this case, results of S-band waveguide are not shown since the operating frequency range of it does not cover 2.5 GHz and the 4GHz used later. It can be seen that the range is set as 800 mm long which is much larger than each antenna aperture size. And position 0 mm means that this point is located at the center of the plane with *z* (depth) equal to 124 mm. The beamwidth of curved horn is much larger than the other two in H-plane and the E-plane beamwidth for all three are about the same. The H-plane beamwidths of the pyramidal horn and Vivaldi antenna are almost equal. The beamwidths of all three antennas are listed in Table 3-5. Similar results were obtained at 4 GHz (not shown).

Table 3-5: Half-power beamwidth (unit: degree) obtained by squaring field distributions in Figure 3-59.

	Frequency	Plane	Curved Horn	Vivaldi	Pyramidal Horn
HPBW (mm)	2.5 GHz	H	246.8	133.9	131.6
		E	116.0	99.6	173.8
	4 GHz	H	204.3	91.4	72.5
		E	105.0	142.3	85.3
Center Magnitude (dB)	2.5 GHz	Center Point	32.2	35.2	35.2
	4 GHz		31.2	31.4	37.6

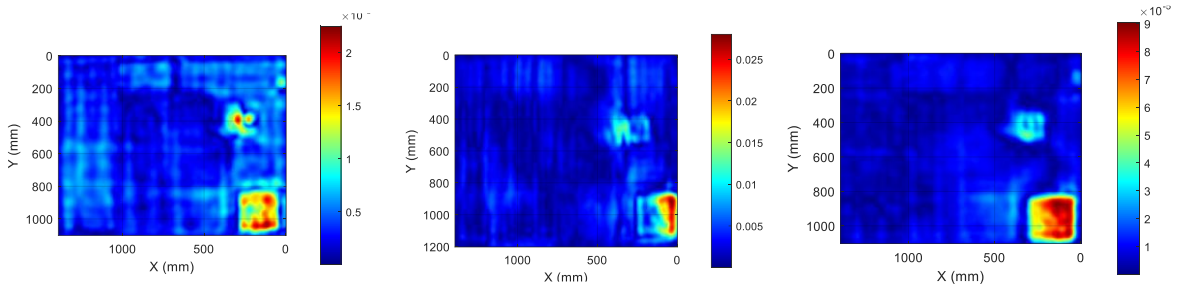

Figure 3-60: Imaging results at 2.5-2.6 GHz, produced by curved Horn (left), produced by pyramidal Horn (middle), produced by Vivaldi antenna (right).

The produced SAR images of the concrete slab at 2.5-2.6 GHz are given in Figure 3-60. For the foam, it can be seen that all the three images can show the presence of the large foam at the right bottom position and the small foam at the right middle position. For delamination simulated by plastic sheets, it can be found from the image of curved horn in Figure 3-60-left, at the top part of the image, there is a square object located between 750 mm and 1000 mm region in X coordinate direction and from 0 to 200 mm in Y coordinate direction. And another two square objects may exist on the left of that plastic square sheet with X approximately ranging from 0 to 300 mm and from 350 mm to 700 mm, respectively. Meanwhile, at the left part of the image, with Y being from 500 mm to 900 mm, one or more square objects are indicated. However, the indications for these plastic sheets in the images of pyramidal horn and Vivaldi antenna are somewhat faint except the plastic sheet left to the large foam at the right bottom corner which cannot be clearly displayed by the image of pyramidal horn but images of curved horn and Vivaldi antenna can. Moreover, at the left part of the image of curved horn in Figure 3-60-left, signals from some rebars can also be observed while the images from the other two antennas cannot.

In conclusion, for the detection of plastic sheets, curved horn can show much more and stronger indications in its image than pyramidal horn and Vivaldi antenna while for the latter two, pyramidal horn can provide somewhat stronger indication than Vivaldi antenna. Consequently, this is expected based on

the field distributions in Figure 3-59 in which curved horn shows much wider beamwidth than the other two in H plane while HPBW of pyramidal horn is slightly larger than the other two in E plane.

Meanwhile, center magnitude, which means the amplitude of electrical field at the center point of the XY plane (perpendicular to depth direction), is also given in Table 3-5. It should be noted that the input power for the three antennas in measurements is 1 Watt while for simulations it is 0.5 Watt. It can be seen that magnitude of Vivaldi antenna and pyramidal horn are close at 2.5 GHz and that of curved horn is smaller than the other two indicating large value magnitude of electrical field is properly not the reason for higher resolution, and wider beamwidth may result in less magnitude of electric field.

In order to show the generality of this phenomenon, similar to the 2.5 GHz case, the field distributions at 4 GHz are given in Figure 3-61, and SAR algorithm is also applied to the raw data obtained at 3.9-4GHz and results of them are displayed in Figure 3-62. As can be seen, the curved horn still has the largest beamwidth.

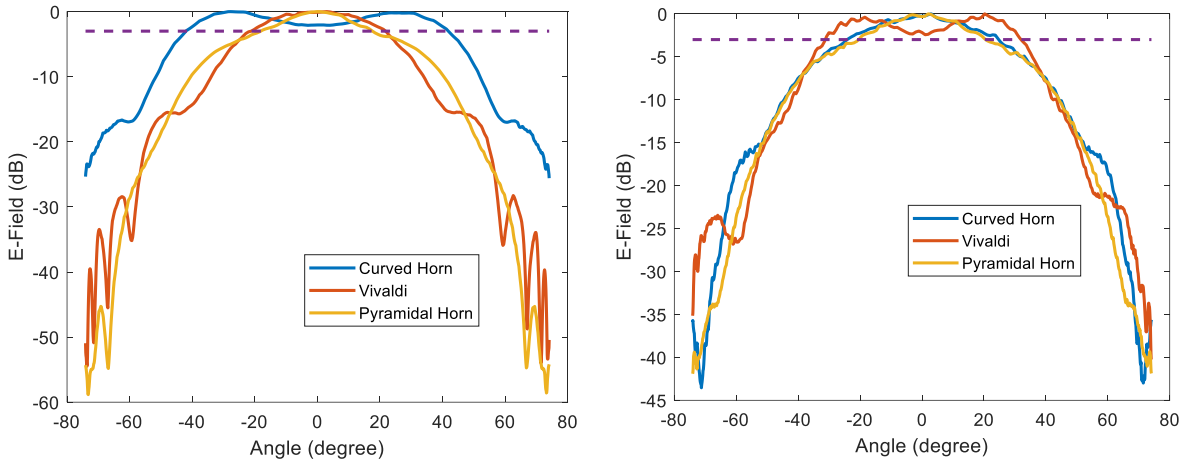

Figure 3-61: Electric field distributions of the three antennas at 4 GHz: H-plane (left), and E-plane (right).

In this case, since the frequency is high in the operating range, sensitivity is hence relatively higher so that it can bring better detectability and consequently more information can be shown in the final images. This expectation can be observed by the three images in Figure 3-62 in which indications on all objects by the three antennas become stronger. In Figure 3-62-left, the unclear signal shown in 2.5-2.6

GHz case around the small foam at the right middle part is removed and only a small circular-shape object is left which is also shown in Figure 3-62-middle and right but with magnitude being weaker gradually. Hence, there should be something there and not noise. After linking it to Figure 3-43, it can be the indication of the small plastic sheet. It is similar phenomenon for the plastic sheets located at the top part and the large plastic sheet located at the right bottom corner left to the large foam.

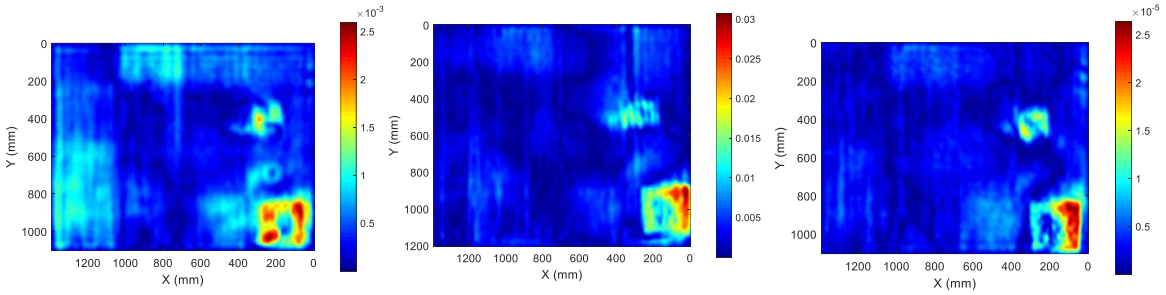

Figure 3-62: Imaging results at 3.9-4 GHz, images are produced by curved horn (left), pyramidal horn (middle), and Vivaldi horn (right)

Meanwhile, at the left part of the image of Figure 3-62-left, signals become even unclear compared with 2.5-2.6 GHz, and cannot be determined as either noise or useful indications so far. Possible reason may be that these plastic sheets are shifted and wrapped together with irregular shape and hence cannot be identified.

For the center magnitude, it can be seen that curved horn has the smallest magnitude and it is close to the value of Vivaldi antenna. This verifies that magnitude may not be responsible for the difference between the SAR images of curved horn and Vivaldi antenna. And the matching properties of Vivaldi antenna from its aperture to concrete may be worse than pyramidal horn since the beamwidth of them are close but center magnitude is different at 4GHz (close at 2.5 GHz).

3.9.4 Antenna pattern effect on SAR sensitivity to delamination

In order to show the above phenomenon in a more accurate and rigorous way, the cross-range resolution, range resolution, and aperture gain as a function of beamwidth are studied. In this case, the nondirectional pattern is easily applied and hence widely used in remote sensing, but it may be not

accurate enough for NDE problems. This can be explained by Figure 3-63, in which the left figure shows cases that an object is located at small depth distance while the right figure shows cases with large depth distance. The dashed line indicated by nondirectional pattern is the antenna gain pattern used previously while the solid line indicated by directional pattern is the real antenna gain pattern. It can be seen that they have large difference at small depth distance cases.

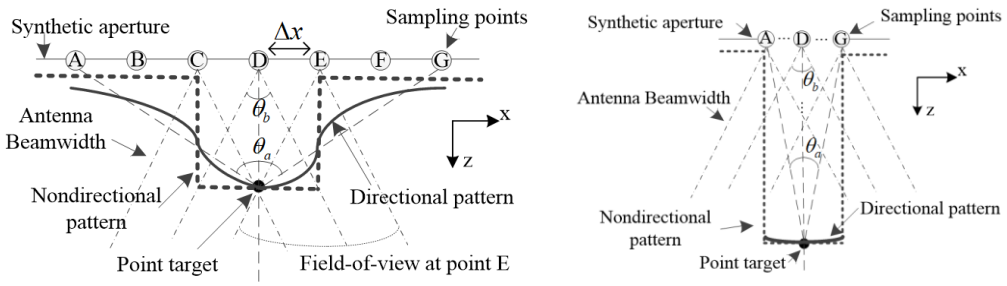

Figure 3-63: Illustration for SAR imaging and antenna patterns, small depth distance (left), large depth distance (right)

3.9.4.1 Cross-range resolution

The simulation setup is given in Figure 3-64 for a point target. the simulated results are obtained by calculating the 3dB width of the square of the reconstructed signal along the cross-range direction.

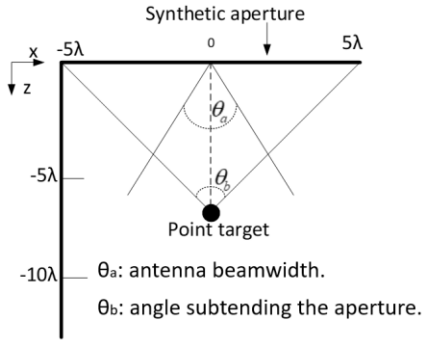

Figure 3-64: Simulation setup for cross-range resolution modelling

Results produced by equation (4) are also used as a reference.

$$\delta_{xc} = \frac{2h\delta_{xo}}{2h+\delta_{xo}} \quad (4)$$

Results are given in Figure 3-65. As can be seen from Figure 3-65-a, in which the ideal 180-degree antenna half power beamwidth (HPBW) is firstly used since this is the simplest case and only the aperture angle works for the SAR system. It shows that the simulation results almost same as the theoretical value except very tiny shift around h=20 λ_c which may be from numerical errors. This indicates the good validity of the simulation system. Then, by changing HPBW to smaller ones to consider HPBW effect as a function of depth, as can be seen from Figure 3-65-b, both simulation and theoretical results also match well. Moreover, unlike the 180-degree HPBW case, curves in Figure 3-65-b show jump points at certain depth as h increases. These indicate that the cross-range resolution is strongly affected by ABW before this point, and after it, the cross-range resolution is determined by the aperture angle and hence curves overlap then.

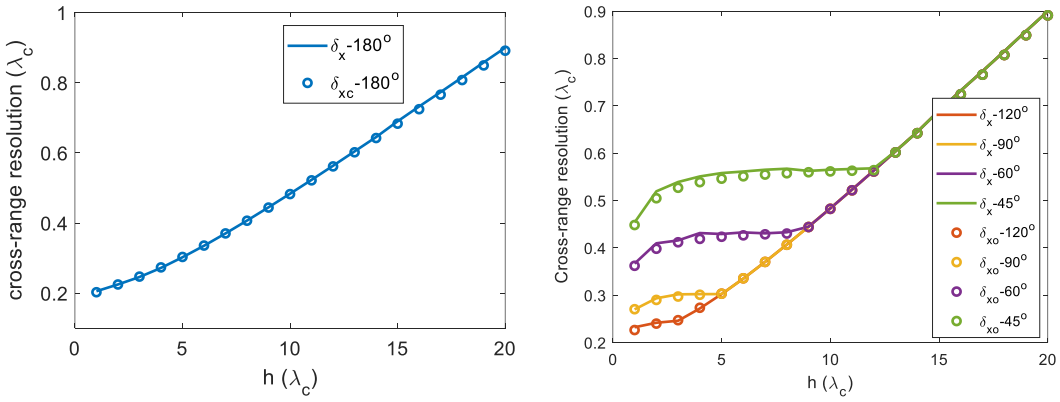

(a) Without pattern effect, ABW=180° (b) With pattern effect

Figure 3-65: Cross-range resolution simulation results using rect pattern

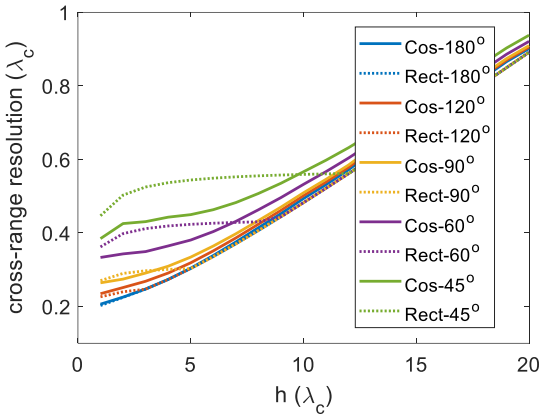

Figure 3-66: cross-range resolution simulation results using *Rect* pattern and cos pattern

Then, the influence of real antenna gain pattern is also considered. Since the gain pattern is usually having the maximum at the θ=0° direction and smallest value at θ=±90° direction, the cos function may be a good option and is hence used here to approximate the real antenna gain pattern. Results for cross-range resolution are given in Figure 3-66. Results from nondirectional patterns (named Rect) are also given as reference. As can be seen from Figure 3-66, at small depth distance (i.e. <5λ_c), the actual cross-range resolution produced by directional pattern is better than the results from nondirectional patterns, especially when the beamwidth is small (i.e 45°). This is expected since the effective aperture length can be efficiently increased by the Cos patterns. And different from results in Figure 3-65, the change of the cross-range resolution has no jump points. Reason for this is that all the sampling points of the synthetic aperture are valid for transmitting and receiving information rather than the *Rect* pattern assumption that some of the sampling points may not work when the point target is out of the beamwidth.

3.9.4.2 Range resolution

The simulated results are obtained by the similar way as in calculating the cross-range resolution, the only difference is that the reconstructed signal along the range direction is used to calculate the range resolution. Results are shown in Figure 3-67, in which δ_z is the simulated range resolution, and δ_{zo} is given by

$$\delta_{zo} = \frac{0.4422\lambda_c}{B_r} \approx \frac{c}{2B} \quad (5)$$

in which B_r is the fractional frequency bandwidth, B is the frequency bandwidth, and c is the speed of light in free space.

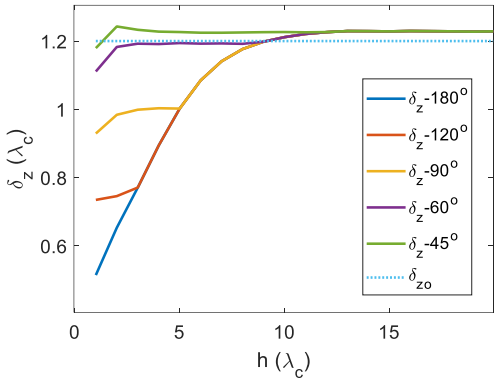

Figure 3-67: Range resolution simulation results using *Rect* pattern

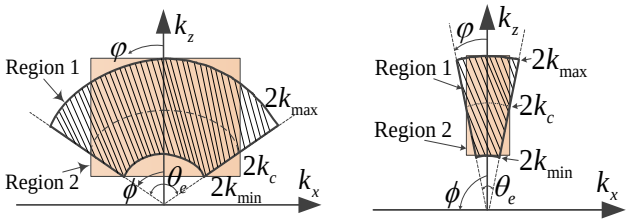

(a) Wide-angle case (b) narrow-angle case

Figure 3-68: Spatial spectrum of SAR

As can be seen from Figure 3-67, for the result using 180° antenna HPBW, the aperture angle is always smaller than the ABW, and hence it limits the effective integration angle and dominates the range resolution. Therefore, the decrease of this aperture angle as depth distance becomes larger leads to the degradation of the range resolution, which finally converges to a value close to δ_{zo}. Since the effective integration angle is large at small depth distance (approximately when h$\leqslant 10\lambda_c$), the spatial spectrum is similar to the case shown in Figure 3-68-a, in which the width in k_z direction is larger than the result of $2k_{max}$-$2k_{min}$, leading to better range resolution than the case shown in Figure 3-68-b which is

with small effective integration angle and corresponds to cases here where h>10λ_c. Then, similar phenomenon can be found from the results produced by 120°, 90°, 60°, and 45° HPBW.

Then, the real gain pattern effect to range resolution is also considered. Results are given in Figure 3-69. Results produced by nondirectional are also given as a comparison. As can be observed, the newly obtained range resolution is much better than that produced by the Rect patterns in most cases. Reason for this may be that the real gain pattern with Cos function distribution can "see" more areas in the range direction based on larger aperture length.

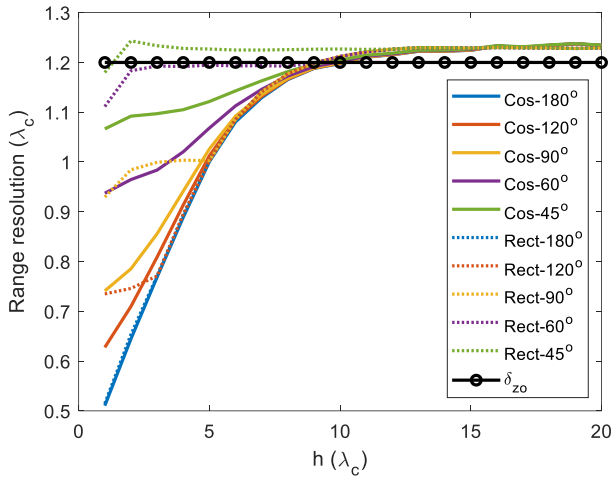

Figure 3-69: Simulated range resolution by cos pattern as function of antenna beamwidth

3.9.4.3 Aperture gain

Next, aperture gain (peak intensity), which may influence the signal-to-noise ratio (SNR) of a SAR imaging system, is also an important parameter to be evaluated. In this case, if the *Rect* patterns used above with different HPBW are assumed to have same power, then the equation for the collated data can be formed by:

$$S_i = {A_j}^2 \cdot rect(\frac{2\theta}{\theta_j}) \cdot \frac{exp\,(-j2kR_i)}{R_i^2} \quad (6)$$

in which $rect(2\theta/\theta_j)$ represents the corresponding jth *Rect* pattern with HPBW θ_j. If the amplitude of antenna gain pattern with HPBW=180o case is assumed to be 1, then its total energy is π since the range of θ is from -π/2 to π/2. Consequently, the amplitude A_j is:

$$A_j = \sqrt{\frac{\pi}{\theta_j}} \tag{7}$$

The simulated results are shown in Figure 3-70-left. All the values are normalized to the maximum of the result with 180° ABW. As can be seen from it, generally, narrow HPBW brings higher peak intensity. Reasons for this include, firstly, even though wide HPBW brings larger effective aperture (since it can illuminate larger area), the contributions from sampling points located far away from the aperture center are gradually weakened due to the $1/R^2$ term. Secondly, the amplitude (A_j) of narrower ABW is higher leading to the fact that more energy can be transmitted out from the sampling points close to the aperture center. Consequently, though wide HPBW can bring high resolution, the peak intensity of the reconstructed image is low. And as depth distance increases, this difference in peak intensity influenced by HPBW will be increased as well. The influence by real antenna gain pattern (approximated by cos function, hence named *Cos* pattern hereafter) to the aperture gain (larger antenna gain leads to narrow beamwidth, narrow beamwidth changes aperture gain) has little difference from this as shown by Figure 3-70-right.

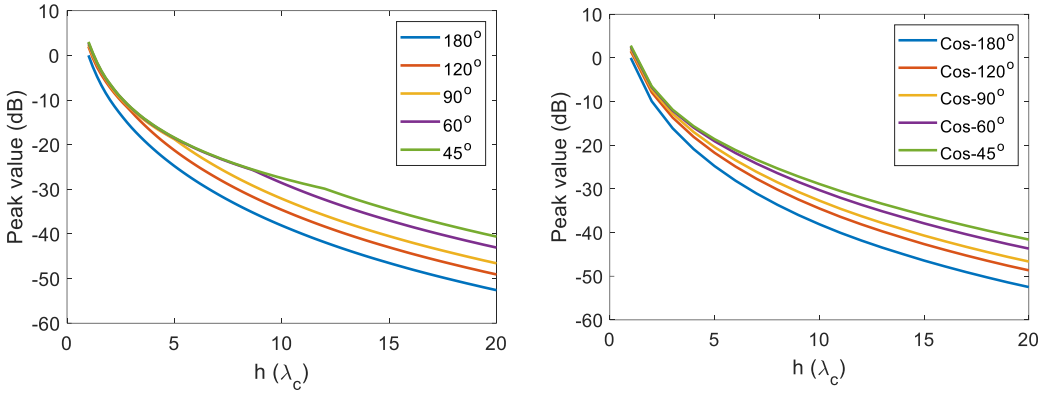

Figure 3-70: Peak intensity using *Rect* pattern (left) and *Cos* pattern (right) with different HPBW

3.9.4.4 Side lobe ratio

Apart from the three parameters discussed above, it was also found that antenna gain pattern can also influence a lot to the side lobe level of the impulse response function (shown in Figure 3-71-left) owing to a SAR system. Simulations were conducted for a point target using different antenna pattern (differing in beam width) ranging from 45.2° to 180°. It can be seen from Figure 3-71-right that the largest side lobe level can be changed a lot by tuning the beamwidth.

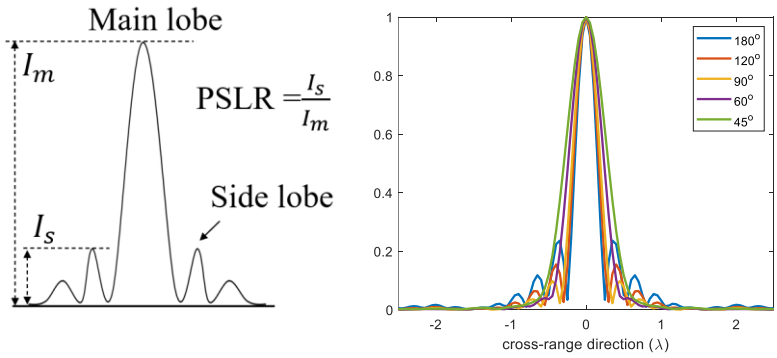

Figure 3-71: Shape of the impulse response function (left), and the reconstructed signals along cross-range direction as a function of beamwidth (right)

Then, to approximate the condition above that strong-scattering and weak-scattering objects are put together, simulation were done by putting a point target with 0.1 reflectivity near another point target with 1.0 reflectivity (both are normalized to 1.0), to see the detectability and also the sensitivity to the first target of a SAR system using different antenna gain patterns. The distance between these two

targets is 0.8 λ_c. The setup is given in Figure 3-72-left, the produced SAR image using 90-degree HPBW of gain pattern is given in Figure 3-72-middle, while the 1D signals (the above mentioned impulse response function) extracted from the produced SAR images along the cross-range direction are given in Figure 3-72-right. It can be observed that weak-scattering object can be detected, but larger beamwidth can bring higher magnitude of it as shown in Figure 3-72-right. This confirms that antenna gain pattern can be responsible for the sensitivity. Finally, the peak side lobe ratio (PSLR) which is given in Figure 3-71-left and defined as the ratio between the largest side lobe peak value over the main lobe peak value, was used to describe the side lobe level, and the change of it as a function of pattern beamwidth and depth distance is given in Figure 3-73. As can be seen from it, smaller pattern beamwidth leads to weaker side lobe ratio, and hence the lower of the sensitivity of the SAR system to the weak-scattering target (nearby a strong-scattering object).

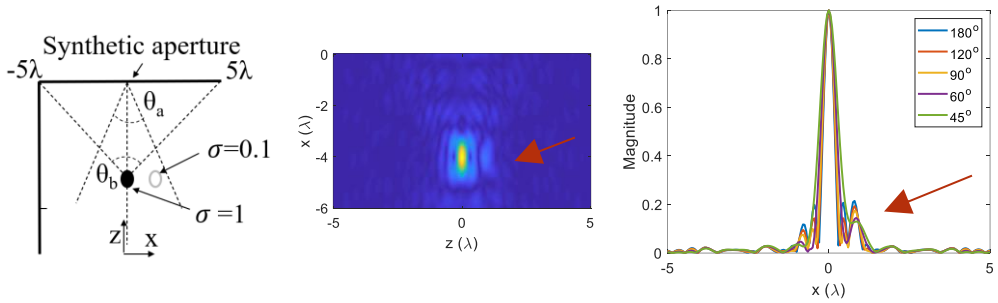

Figure 3-72: Simulation setup (left), reconstructed image (middle), and the extracted signalsfrom the produced SAR images along the cross-range (x) direction as a function of antenna pattern beamwidth (right).

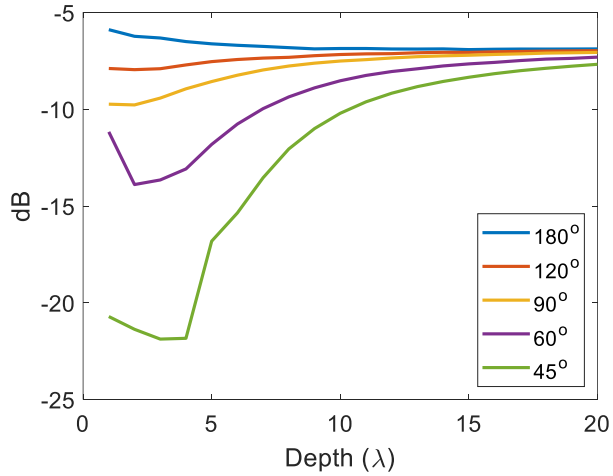

Figure 3-73: PSLR as a function of the beamwidth of antenna pattern and depth distance.

3.9.4.5 Measurement verification

In order to confirm the correctness of the above simulation, measurements were done by using a metal wire with a diameter of 0.6 mm (i.e., < 0.1λ) as the point target. This wire, when sufficiently long, acts as a point target when scanned along a direction orthogonal to its length. An open-ended rectangular waveguide probe, operating at Ku-band (12.8-18 GHz), was used as the scanning antenna. this probe has the added advantage that it can be calibrated using standard loads and procedures. The entire measurement setup is shown in Figure 3-74. The structure holding the wire (i.e., the books) were sufficiently away from each other and cause no additional reflections. The wire was stretched straight and held 240 mm (i.e., > 12λ_c) above the surface of the scanning platform. The irradiating electric filed polarization direction was parallel to the wire. Subsequently, the wire was raster scanned in the direction orthogonal to the length of the wire with 401 frequency sampling points recorded (scanned along the *x* direction), with a sampling step size of 0.05λ_c, consistent with that in the simulations.

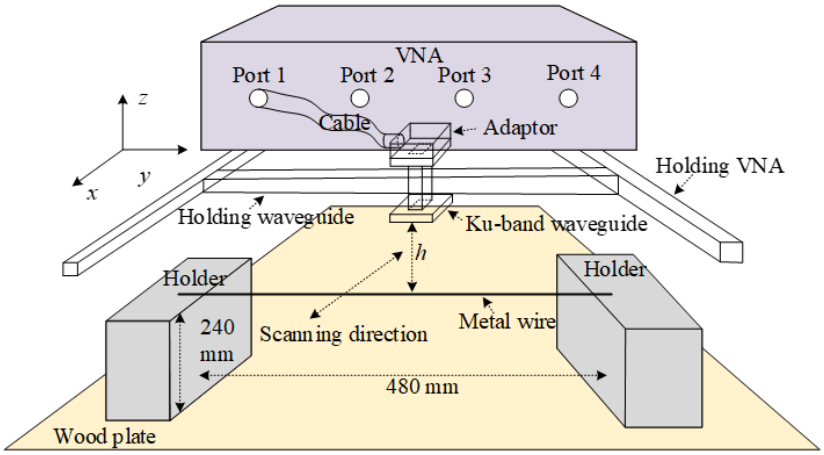

Figure 3-74: Schematic of the measurement setup.

In this case, the measurement results are given in Figure 3-75, which shows the comparison between these and the simulation results for cross-range resolution, range resolution and PSLR. Moreover, the depth range $2\lambda_c$~$7\lambda_c$ is used since both the cross-range and the range resolution have strong dependence on the antenna gain pattern within this range predicted by the simulation results.

For cross-range resolution, as can be seen in Figure 3-75-a, the simulation results from the *Rect* and the *Cos* patterns are slightly different, particularly for shorter target depths, and the results converge as the target depth increases. However, the measured results closely match those obtained from the *Cos* pattern. A similar trend is observed for range resolution in Figure 3-75-b, with a more substantial difference between the simulation results for the non-directional and the directional patterns, while the measured results closely match those from the directional pattern.

With respect to the sidelobe level, as can be seen in Figure 3-75-c, the simulation results for the *Rect* and the *Cos* patterns do not closely match. The *Rect* pattern is expected to produce lower PSLR with increasing depth while for the *Cos* pattern, the PSLR is expected increases quickly at smaller depths (except at $h = \lambda$) and then slowly increase at larger depths. However, the measured data behaves

similarly to that obtained from the directional pattern, to within only 2 dB, verifying the validity of the proposed method.

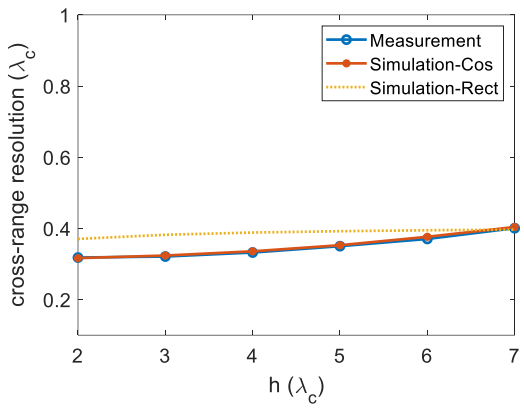

(a) cross-range resolution

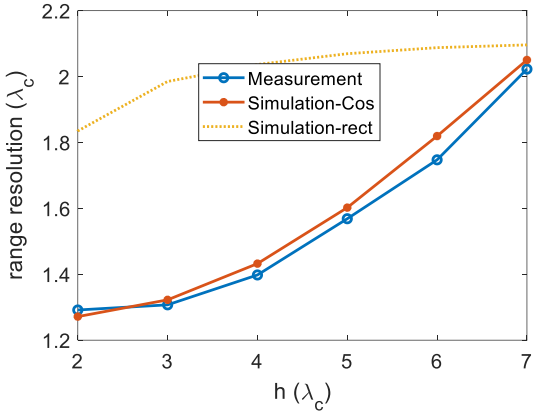

(b) range resolution

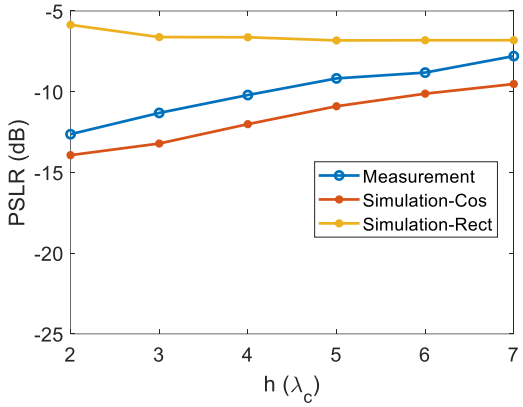

(c) PSLR

Figure 3-75: SAR imaging measurement results using the Ku-band open-ended waveguide probe in the 14.8-16.8 GHz frequency range.

Chapter 4 **FINDINGS**

Based on the work mentioned above, we have three relatively important findings, as enumerated below.

4.1 Sensitivity of microwave SAR imaging technique to corrosion thickness

It has been verified by simulations that microwave SAR imaging technique employing advanced multilayer SAR algorithm can quantitatively detect the corrosion thickness as small as 5% of corrosion

[17]. However, for 0.2% corrosion thickness which occurred in these experiments, microwave SAR imaging technique did not seem to able to detect that level of corrosion. We also believe the samples utilized in this work may not have been prepared in a way to help these measurements, as some generated large crack rather quickly.

4.2 Sensitivity of microwave SAR imaging technique to concrete delamination

Based on our study, it has been found that the detectability of microwave SAR imaging system to different kind of delamination objects are different. One reason is by the resolution, since objects with smaller size are always more difficult to detect than larger ones. Another reason is the difference in scattering property. For example, assuming same size objects but one is strong scattering and another one is weak scattering, then, the former one is always easier to be detected. This led to discovering that antenna beamwidth can be used to tune such sensitivity. The conclusion is that in order to detect most kinds of objects in concrete, the beamwidth can be continuously changed to do a scanning about detecting delamination with different scattering capability. It must also be mentioned that the delamination sample prepared did not end up having the desired characteristics (i.e.k,some of the defect moved from their designed locations).

Using a hand-scanning process a pedestrian bridge on the campus of MO S&T was imaged, and many indications were detected. Given there is ground-truth data on the state of the bridge we could not collaborate the results.

4.3 Sensitivity of microwave harmonic measurement to corrosion detection

It was also discovered that microwave harmonic measurement scan be an efficient tool for corrosion monitoring. Different from microwave SAR imaging technique, nonlinear components of scattered field may be used for detecting corrosion. But, it appeared that this method worked better on to exposed rebars than any embedded ones.

Chapter 5 **5. CONCLUSIONS**

In conclusion, we believe SAR imaging still has tremendous applicability to detecting corrosion on rebars. However, a bet set of "critical flaw size" must be established, in which case it can be determined whether the method is ultimately incapable of corrosion detecting of less 1%. For the result of concluding remarks please refer to Section 4.

Chapter 6 **6. RECOMMENDATIONS DEVELOPED AS A RESULT OF THE PROJECT**

(1) Corrosion thickness of a rebar embedded into concrete may have been to thin small (50 μm level), different from reported 20% corrosion percentage in literature [19]. It may be concluded that microwave SAR imaging technique operating in the cm-wave may not possess such a capability. At higher frequencies, the signal penetration becomes a limiting factor. In any future potential investigation, much care should eb paid to how samples are case and corroded

(2) Microwave SAR imaging technique is an efficient tool for concrete delamination detection. Different kinds of delamination can be detected by tuning the parameters in SAR imaging system.

(3) Microwave harmonic measurement is a potential tool for corrosion monitoring since it has experimental confirmed with high sensitivity to corrosion at the rebar-rebar junction. This I something that may be investigated in the future.

Chapter 7 **References**

[1] Koch, G.H., Brongers, M.P.H., Thompson, N.G., Virmani, Y.P., and Payer, J.H., "Corrosion Costs and Preventive Strategies in the United States," Report FHWA-RD-01-156, report by CC Technologies Laboratories, Inc. to Federal Highway Administration (FHWA), Office of Infrastructure Research and Development, p. 784, 2001.

[2] ACI Committee 228, "Nondestructive Test Methods for Evaluation of Concrete in Structures (ACI 228.2R-98),

American Concrete Institute, Farmington Hills, MI, p. 62, 1998 (Reapproved 2004).
[3] Poursaee, A., "An Analysis of the Factors Influencing Electrochemical Measurements of the Condition of Reinforcing Steel in Concrete Structures," Ph.D. Thesis, University of Waterloo, Waterloo, ON, Canada, p. 298, 2007.
[4] Flis, J., Sabol, S., Pickering, H., Seghal, A.; Osseo-Asare, K., and Cady, P., "Electrochemical Measurements on Concrete Bridges for Evaluation of Reinforcement Corrosion Rates," Corrosion, V. 49, No. 7, pp. 601-613, 1993.
[5] Malhotra, V.M., and Carino, N.J., Handbook on Nondestructive Testing of Concrete, second edition, CRC Press, Boca Raton, FL, 2004.
[6] Poursaee, A., "Corrosion Measurement Techniques in Steel Reinforced Concrete," Journal of ASTM International, vol. 8, no. 5, pp. 1-15, 2011.
[7] Fallahpour, M., Case, J. T., Ghasr, M.T., and Zoughi, R., "Piecewise and Wiener filter-based SAR techniques for monostatic microwave imaging of layered structures," IEEE Transactions Antennas Propagation, vol. 62, no. 1, pp. 282–294, 2014.
[8] D. Sheen, D. McMakin, and T. E. Hall, "Three-dimensional millimeterwave imaging for concealed weapon detection," IEEE Trans. MTT, vol. 49, no. 9, pp. 1581–1592, 2001.
[9] Case, J.T., M.T. Ghasr, M.T., R. Zoughi, "Optimum two-dimensional uniform spatial sampling for microwave SAR-based NDE imaging systems", IEEE Trans.Instrum. Meas., 2011, 60, (12), pp. 3806–3815.
[10] Munk, B. A. Frequency Selective Surfaces: Theory and Design (Wiley, 2000).
[11] K. Zhang, T. Li, and J. Jiang, "Passive intermodulation of contact nonlinearity on microwave connector," IEEE Trans. Electromagn. Compat., vol. 60, no. 2, pp. 513–519, Apr. 2018.
[12] J. W. You, J. F. Zhang, W. H. Gu, W. Z. Cui and T. J. Cui, "Numerical Analysis of Passive Intermodulation Arisen From Nonlinear Contacts in HPMW Devices," in IEEE Transactions on Electromagnetic Compatibility, vol. 60, no. 5, pp. 1470-1480, Oct. 2018, doi: 10.1109/TEMC.2017.2761024.
[13] S. Grover, G. Moddel, Metal single-insulator and multi-insulator diodes for rectenna solar cells, in: G. Moddel, S. Grover (Eds.), Rectenna Solar Cells, Springer New York, 2013, pp. 89–109.
[14] Liu, C.; Barker, S.; Fan, L.; Ghasr, M.T.A.; Chen, G.; Zoughi, R. Microwave High-Resolution 3D SAR Imaging of Corroded Reinforcing Steel Bars in Mortar Subjected to Accelerated Electrochemical Corrosion. In Proceedings of the International Conference on Structural Health Monitoring of Intelligent Infrastructure, St. Louis, MO, USA, 4–7 August 2019.
[15] Bois, K., L. Handjojo, A. Benally, K. Mubarak and R. Zoughi, "Dielectric Plug-Loaded Two-Port Transmission Line Measurement Technique for Dielectric Property Characterization of Granular and Liquid Materials," IEEE Transactions on Instrumentation and Measurement, vol. 48, no. 6, pp. 1141-1148, December 1999.
[16] Qaddoumi, N., Handjojo, L., Bigelow, T., Easter, J., Bray, A., & Zoughi, R. (2000). Microwave corrosion detection using open ended rectangular waveguide sensors. Materials Evaluation, 58(2).
[17] Ghasr, M.T., Y. LePape, D.B. Scott, and R. Zoughi, "Holographical Microwave Imaging of Corroded Steel Bars in Concrete," *American Concrete Institute (ACI) Materials Journal*, vol. 112, no. 1, pp. 115-124, January 2015.
[18] Mosig, J.R., Melcon, A.A., "Green's functions in lossy layered media: integration along the imaginary axis and asymptotic behavior," IEEE Transactions Antennas Propagation., vol. 51, pp. 3200–3208, 2003.
[19] G. Roqueta, L. Jofre and M. Q. Feng, "Analysis of the Electromagnetic Signature of Reinforced Concrete Structures for Nondestructive Evaluation of Corrosion Damage," in *IEEE Transactions on Instrumentation and Measurement*, vol. 61, no. 4, pp. 1090-1098, April 2012, doi: 10.1109/TIM.2011.2174106.